Remote Sensing of Environment 156 (2015) 473–489

Contents lists available at ScienceDirect

Remote Sensing of Environment

journal homepage: www.elsevier.com/locate/rse

Comparison of new and primary production models using SeaWiFS data in contrasting hydrographic zones of the northern North Atlantic

Gavin H. Tilstone [a,*], Benjamin H. Taylor [a], David Blondeau-Patissier [b,c], Tim Powell [a], Steve B. Groom [a], Andrew P. Rees [a], Mike I. Lucas [d]

[a] Plymouth Marine Laboratory, Prospect Place, West Hoe, Plymouth PL1 3DH, UK
[b] North Australia Marine Research Alliance (NAMRA), Charles Darwin University, Darwin, Australia
[c] Research Institute for the Environment and Livelihoods (RIEL), Charles Darwin University, Darwin, Australia
[d] Department of Biological Sciences, University of Cape Town, Private Bag, Rondebosch 7701, South Africa

ARTICLE INFO

Article history:
Received 12 January 2014
Received in revised form 9 October 2014
Accepted 15 October 2014
Available online 6 November 2014

Keywords:
Phytoplankton
Primary production
New production
Ocean Colour
North Atlantic
Arctic Oscillation
North Atlantic Oscillation

ABSTRACT

The accuracy of two satellite models of marine primary (PP) and new production (NP) were assessed against ^{14}C and ^{15}N uptake measurements taken during six research cruises in the northern North Atlantic. The wavelength resolving model (WRM) was more accurate than the Vertical General Production Model (VGPM) for computation of both PP and NP. Mean monthly satellite maps of PP and NP for both models were generated from 1997 to 2010 using SeaWiFS data for the Irminger basin and North Atlantic. Intra- and inter-annual variability of the two models was compared in six hydrographic zones. Both models exhibited similar spatio-temporal patterns: PP and NP increased from April to June and decreased by August. Higher values were associated with the East Greenland Current (EGC), Iceland Basin (ICB) and the Reykjanes Ridge (RKR) and lower values occurred in the Central Irminger Current (CIC), North Irminger Current (NIC) and Southern Irminger Current (SIC). The annual PP and NP over the SeaWiFS record was 258 and 82 gC m^{-2} yr^{-1} respectively for the VGPM and 190 and 41 gC m^{-2} yr^{-1} for the WRM. Average annual cumulative sum in the anomalies of NP for the VGPM were positively correlated with the North Atlantic Oscillation (NAO) in the EGC, CIC and SIC and negatively correlated with the multivariate ENSO index (MEI) in the ICB. By contrast, cumulative sum of the anomalies of NP for the WRM were significantly correlated with NAO only in the EGC and CIC. NP from both VGPM and WRM exhibited significant negative correlations with Arctic Oscillation (AO) in all hydrographic zones. The differences in estimates of PP and NP in these hydrographic zones arise principally from the parameterisation of the euphotic depth and the SST dependence of photo-physiological term in the VGPM, which has a greater sensitivity to variations in temperature than the WRM. In waters of 0 to 5 °C PP using the VGPM was 43% higher than WRM, from 5 to 10 °C the VGPM was 29% higher and from 10 to 15 °C the VGPM was 27% higher.

1. Introduction

Recent warming of the Global Ocean has potentially important impacts on carbon cycling in the marine ecosystem, which is hard to quantify due to the scarcity of data over both space and time. Recent advances in Earth Observation (EO) have enabled us to fill these gaps, but the accuracy of satellite models requires careful consideration if we are to employ them to quantify the carbon fluxes in an ecosystem.

Quantitative estimation of the draw-down of carbon dioxide from the atmosphere to the ocean via primary production (PP) and the exported fraction of this fixed carbon, is important for calculating the global CO_2 flux and for modeling carbon transfer through the pelagic food web to the deep sea (Azam, 1998; Falkowski, 1988; Sarmiento, Hughes, Stouffer, & Manabe, 1998). NP is that proportion of PP driven by allocthonous nutrients that are supplied to the ecosystem through physical processes, nitrogen fixation or atmospheric input (Dugdale & Goering, 1967; Yentsch, Yentsch, Phinney, Lapointe, & Yentsch, 2004). The remaining fraction, the regenerated production, is driven by nutrients produced by re-mineralisation processes which include ammonification (Dugdale & Goering, 1967) and nitrification (Yool, Martin, Fernandez, & Clark, 2007) within the euphotic zone. It is balanced by export to deep waters or higher trophic levels, and makes a direct contribution to carbon removal from the photic zone. The measurement of NP is conventionally based on the uptake of ^{15}N-labelled nitrogen (NO_3^-, NH_4^+, urea), which has undoubtedly aided our understanding of the global importance of the world's oceans in exporting carbon. In many regions, few NP measurements are available resulting in sparse spatial and temporal data coverage and a vague impression of

* Corresponding author. Tel.: +44 1752 633406; fax: +44 1752 633101.
URL: http://ghti@pml.ac.uk (G.H. Tilstone).

http://dx.doi.org/10.1016/j.rse.2014.10.013
0034-4257/

phytoplankton NP dynamics. There has, therefore, been a concerted effort to derive accurate estimates of NP from satellite data to fill this gap (Falkowski, 1988; Laws, Falkowski, Smith, Ducklow, & McCarthy, 2000). These have been aided by the inverse relationship between temperature and nutrients in certain regions of the Atlantic and Pacific (Chavez, Service, & Buttrey, 1996; Goes et al., 2000; Morin, Wafar, & Lecorre, 1993; Sathyendranath, Gouveia, Shetye, Ravindran, & Platt, 1991), particularly in upwelling and tidally driven areas (Babin, Therriault, & Legendre, 1991; Dugdale, Morel, Bricaud, & Wilkerson, 1989; Morin et al., 1993; Waldron & Probyn, 1992), to enable the determination of large-scale estimates of NP from satellite Sea Surface Temperature (SST) data (Alvarez-Salgado et al., 2002; Dugdale, Davis, & Wilkerson, 1997; Kamykowski, Reed, & Kirkpatrick, 1992; Traganza, Nestor, & McDonald, 1980). The relationship between SST and nitrate breaks down however, when the water column becomes thermally stratified (Henson, Sanders, Allen, Robinson, & Brown, 2003). Under these scenarios, NP can be underestimated by >50% especially when PP exceeds ~700 mg C m^{-2} d^{-1} (Laws, 2004). Goes, Saino, Oaku, and Jiang (1999), Goes et al. (2000) thus developed an approach to derive NP for the Pacific basin that accounts for phytoplankton consumption of nitrate using a second order polynomial of SST and SeaWiFS Chlorophyll-a (Chla). The algorithm has been used accurately to study the effects of El Niño and land mass warming on NP in the Pacific (Goes, Gomes, Limsakul, Balch, & Saino, 2001) and the Arabian sea (Goes, Gomes, Limsakul, & Saino, 2004). Similarly, Laws et al. (2000) developed a food web model that can be used to predict export production from SST and PP. In this model, the ratio between NP and PP (f-ratio) is temperature-dependent and accounts for 86% of the variability in f-ratios derived from ^{15}N and ^{14}C uptake measurements. In the Pacific upwelling region, when PP is <850 mg C m^{-2} d^{-1} this method is accurate to 10–20% (Laws, 2004), but requires further validation in the Atlantic Ocean, especially at extreme northerly latitudes where few in situ data are available.

The Irminger Basin, located to the Southwest of Iceland and to the Southeast of Greenland, is an important source of export production for the North Atlantic and North Sea (deYoung et al., 2004). From satellite-derived chlorophyll concentrations, NP in the Irminger Basin is predicted to be high ~100–150 gC m^{-2} yr^{-1} (Falkowski, 1988; Laws et al., 2000) and therefore potentially important on a global scale. However, lower values of NP ~30 to 65 gC m^{-2} yr^{-1} have been predicted from in situ nutrient uptake (Henson, Sanders, Holeton, & Allen, 2006; Sanders, Brown, Henson, & Lucas, 2005; Waniek & Holliday, 2006). Recently, Henson et al. (2011) developed a model of export production based on PP and SST and their relationship with thorium (^{234}Th) derived export, which proved to be 60% lower than the e/f-ratio based estimate. Controversy therefore still exists as to the most accurate and appropriate model to estimate NP in this region, which is hampered by a lack of independent in situ observations.

Over the past two decades NASA have conducted five inter-comparisons of satellite models of PP, to determine the most accurate models and to characterise sources of error (Campbell et al., 2002; Carr et al., 2006; Friedrichs et al., 2009; Saba et al., 2010, 2011). Few inter-comparisons of satellite derived NP have been conducted (Silio-Calzada, Bricaud, Uitz, & Gentili, 2008). In a recent error analysis in computation of net PP using the vertical generalised production model (VGPM), Milutinovic and Bertino (2011) quantified the highest uncertainty to be in the northern North Atlantic (>70%) due to errors in irradiance-depth dependent and photosynthetic rate functions.

In this paper we compare the accuracy of two satellite models, the VGPM of Behrenfeld and Falkowski (1997) and a Wavelength Resolved model (WRM) of Morel (1991) at estimating PP and NP in the northern North Atlantic. Each model is used to generate a time series of PP and NP from 1997 to 2010 using SeaWiFS data for six hydrographic zones. Inter-annual differences between models are assessed and in relation to climate indices. A sensitivity analysis was performed to assess which parameters contribute most to errors in the models.

2. Methods

2.1. Study areas and sampling regimes

Integrated PP was derived from ^{14}C uptake measurements at 83 stations on six field campaigns in the Atlantic basin (D261, D264, D267, FISHES, JC011, JC037) and ^{15}N uptake NP measurements were made at 18 stations on two of these campaigns (D261, FISHES) (Fig. 1, Table 1). On all research cruises, vertical profiles of temperature, conductivity, fluorescence, oxygen and photosynthetically active radiation (PAR) were acquired using a Seabird 911 + CTD and Chelsea Instruments PAR sensor fitted to a rosette with either 24 × 20 dm^3 or 12 × 30 dm^3 Niskin-type sampling bottles to collect water samples for the determination of NP, PP, Chla, dissolved inorganic nutrients and photosynthetic parameters (described below). Euphotic depth (Z_{eu}) was determined from the CTD profiles of PAR. The field measurements were used to validate satellite models of PP and NP, which were then applied to the Irminger Sea and northern North Atlantic.

The Irminger Sea is a diverse region with influences from the subtropical thermocline via the North Atlantic Current, and from the Arctic via the dense northern overflows (Holliday et al., 2006), which in turn may influence new production. A number of major physical zones have been described where different surface mixing and re-stratification processes dominate (Holliday et al., 2006; Waniek & Holliday, 2006): The Central Irminger Current (CIC) has characteristically low temperatures and salinity (6.53–9.72 °C, 34.73–35.08) and its surface waters are dominated by cool fresh Sub-Arctic surface water that originates in the Labrador Sea and spreads across the sub-polar gyre. The Irminger Current Zone, a branch of the North Atlantic Current positioned west of the mid-Atlantic Ridge, is the warmest and most saline (7 °C, 35.00) feature of the true Irminger Sea. Two Irminger Current zones are described: The southern Irminger Current (SIC) zone extends from 54–57°N to 60°N and between 28 & 32°W. The North Irminger Current (NIC) occurs between 60 & 62°N and 28 & 32°W. The East Greenland Current Zone (EGC) dominates the western part of the Irminger Sea, including the continental shelf. The EGC is persistent along the length of the Greenland continental slope, carrying cold, fresh (<0 °C, <34.50) Arctic Polar Water and Arctic Intermediate Water (0–3 °C) from the Arctic and Nordic Seas into the sub-polar gyre (Foldvik, Aagaard, & Torresen, 1988). The Reykjanes Ridge (RKR) separates the Irminger Basin from the Iceland Basin (ICB), and is characterised by warm, saline (>8.0 °C, 35.10) water originating from the Iceland basin. The western boundary of the zone is clearly marked by a sharp front with high salinity and temperature gradients, and a distinctive change to weaker stratification and lower density compared to the adjacent Irminger Current.

2.2. Phytoplankton pigments

Chla was determined by high performance liquid chromatography (HPLC) on all field campaigns. Water samples were filtered through Whatman GF/F filters and stored in liquid nitrogen. Pigments were extracted with the aid of sonification in 90% acetone, clarified using centrifugation (5 min at 4000 r.p.m) and analysed in the laboratory, using reverse phase HPLC following the procedure outlined in Barlow, Cummings, and Gibb (1997). Pigments were separated using a 3 μm Hypersil MOS2 C8 column on a Thermo separations product HPLC, detected by absorbance at 440 nm and identified by retention time and on line diode array spectroscopy. Pigment absorption was measured against quantified standards: Chla standard was obtained from Sigma-Aldrich, and divinyl chlorophylls *a* and *b* from R. Bidigare and M. Ondrusek, University of Hawaii. Other pigment standards were purchased from the DHI Institute for Water and Environment, Denmark. Limits of detection were of the order of 0.001 mg m^{-3} (Barlow, Aiken, Moore, Holligan, & Lavender, 2004).

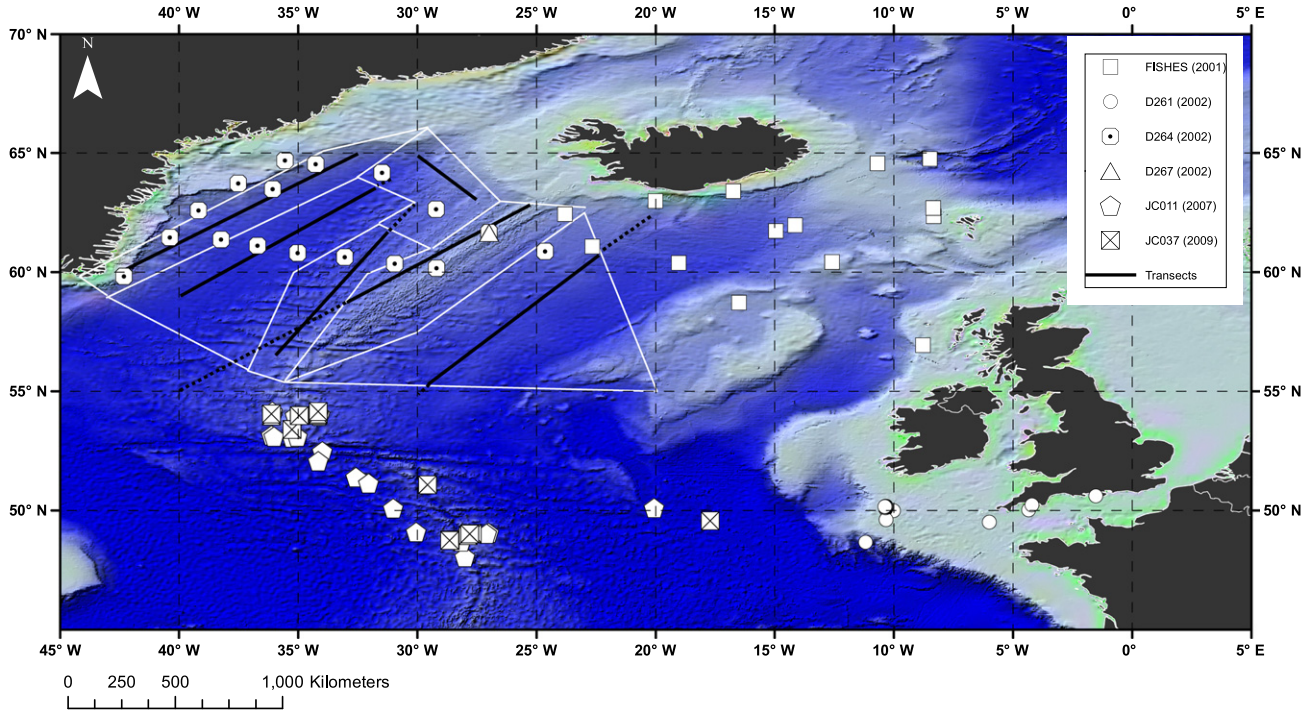

Fig. 1. Sampling stations for primary and new production on research Cruises D261, D264, D267, FISHES, JC011 and JC037 (see Methods section for further details). Location of hydrographic zones are outlined by white lines; EGC is East Greenland Current, NIC is North Irminger Current, CIC is Central Irminger Sea, SIC is South Irminger Current, RKR is Reykjanes Ridge and ICB is Iceland Basin. PP was determined at all stations; NP was determined on FISHES and D261, only. Solid lines are transects from which data were extracted for Fig. 11.

2.3. Simulated in situ ^{14}C primary production

For field campaigns D264, D267 and FISHES, water samples were taken from 6 to 9 depths and transferred from Niskin bottles to blackout carboys to prevent shock to the photosynthetic apparatus of the phytoplankton cells. Water from each sample was sub-sampled into three 75 mL clear and one black, pre-HCl cleaned polycarbonate bottle. Each sample was inoculated with between 185 and 370 kBq (5–10 μCi) $NaH^{14}CO_3$ according to the biomass of phytoplankton. The bottles were transferred to an on-deck simulated in situ (SIS) incubation system which uses neutral density and blue filters to simulate subsurface irradiance over depth to 97%, 55%, 33%, 20%, 14%, 7%, 3%, 1% or 0.1% of the surface value. The samples were matched to the irradiance levels in the incubator and were maintained at near-surface temperature by pumping sea water from a depth of ~7 m through the system. After 24 h incubation from pre-dawn to pre-dawn of the next day, the water samples were filtered through Whatman GF/F filters. The filters were exposed to concentrated HCl fumes for 12 h and then immersed in 2.5 mL scintillation cocktail. ^{14}C disintegration time per minute (DPM) was measured on board using Beckman LS6000 (FISHES, D261, D264, D267), TriCarb 2900 TR (JC037) and Wallac 4040 (JC011) liquid scintillation counter (LSC) using the external standard and the channel ratio methods to correct for quenching. The quantity of ^{14}C added to the experimental bottles was determined by adding aliquots of the stock ^{14}C solution to a CO_2 absorbing scintillation cocktail, which was counted immediately on the LSC. The ^{14}C fixed from dawn to dawn of the following day, was integrated to 1% irradiance depth.

For research cruises D261, JC011 and JC037, photosynthesis-irradiance (PE) experiments were conducted in photosynthetrons illuminated by 50 W, 12 V tungsten halogen lamps following the methods described in Tilstone, Figueiras, Lorenzo, and Arbones (2003). Each incubator houses 14 sub-samples in 0.125 L polycarbonate bottles (Arbones, Figueiras, & Varela, 2000) which were inoculated with between 185 k Bq (5 μCi) and 370 kBq (10 μCi) of ^{14}C labelled bicarbonate. All bottles were pre cleaned following JGOFS protocols (IOC, 1994) to reduce trace metal contamination. The samples were maintained at ambient temperature using a digital temperature controller. After 1 to 2 h of incubation, the suspended material was filtered through Whatman GF/F filters at a vacuum pressure of <20 cm Hg and the filters were then exposed to concentrated HCl fumes for 12 h and immersed in 2.5 ml scintillation cocktail and counted as above. The broadband light-saturated Chla-specific rate of photosynthesis P_m^B[mg C (mg chl a)$^{-1}$ h^{-1}] and the light limited slope α^B[mg C (mg chl a)$^{-1}$ h^{-1} (μmol m^{-2} s^{-1})$^{-1}$] were estimated by fitting the data to the model of Platt, Gallegos, and Harrison (1980), as follows:

$$P_z^B = P_s^B\left[1-\exp\left(-\alpha^B \cdot E_{PAR}/P_s^B\right)\right]\cdot \exp\left(-\beta^B \cdot E_{PAR}/P_s^B\right) \quad (1)$$

Table 1
Location and dates of cruises for the collection of in situ primary production (PP) and new production (NP) data.

Cruise name	Vessel	Dates	Location	Number stations	Reference
FISHES D253	*RRS Discovery*	04 May–20 June 2001	Iceland Basin;	PP = 10, NP = 10	Moore et al. (2005)
D261	*RRS Discovery*	1–14 April 2002	Celtic Sea; 48°N, 5°W to 51°N, 12°W	PP = 16, NP = 8	Robinson et al. (2009)
D264	*RRS Discovery*	30 July–23 Aug 2002.	Irminger Basin;	PP = 15	Holliday et al. (2006)
D267	*RRS Discovery*	15–22 Nov 2002.	Irminger Basin;	PP = 5	Waniek and Holliday (2006)
JC011	*RRS James Cook*	13 July–18 Aug 2007	North Atlantic; 49°N, 28°W to 54°N, 34°W	PP = 19	Read, Pollard, Miller, and Dale (2010)
JC037	*RRS James Cook*	5 Aug–3 Sept 2009	North Atlantic; 49°N, 28°W to 54°N, 34°W	PP = 18	Abell, Brand, Dale, Tilstone, and Beveridge (2013)

where P_z^B is the chlorophyll-specific rate of photosynthesis [mg C (mg Chla)$^{-1}$ h^{-1}] and β^B is the coefficient of photoinhibition [mg C (mg Chla)$^{-1}$ h^{-1} (μmol m^{-2} s^{-1})$^{-1}$] at each given depth. The PAR absorbed by phytoplankton i.e. the photosynthetically usable radiation [E_{PUR} (μmol m^{-3} s^{-1})] at each position in the incubator and for each sampling depth was estimated according to Dubinsky (1980) using measurements of $a_{ph}(\lambda)$. The maximum quantum yield of carbon fixation [ϕ_m mol C fixed (mol photons absorbed)$^{-1}$] was determined by fitting the Chla-specific photosynthetic rates P_z^B [mg C (mg chl a)$^{-1}$ h^{-1}] to E_{PUR} following Figueiras, Arbones, and Estrada (1999). The daily integrated PP (mgC m^{-2} d^{-1}) was estimated using a bio-optical model which inputs E_{PUR}, Chla, P_m^B and ϕ_m to integrate PP at minute by minute intervals, down to 0.1% irradiance depth following Tilstone et al. (2003) as follows:

$$PP_{(PUR)} = \int_{T=0}^{24} \int_{Z=0}^{Z0.1\%} Chla(z) P_m^B(z) \left[1 - \exp\left(-E_{PUR}(t,z)/E_{K(PUR)}(z)\right)\right] dz.dt \quad (2)$$

The SIS determination of PP is closer to net PP as the 24 h incubations account for the dark respiration phase of carbon fixation, whereas the PE method is closer to gross PP as respired carbon is not accounted for during the short term incubation (Marra, 2009). To account for the discrepancy between the two methods, we reduced the PE method estimates by 20% following Joint et al. (2002), as an estimation of carbon loss through the dark phase of photosynthesis.

2.4. in situ ^{15}N new production ($NP_{(IS)}$)

Assimilation rates for NO_3^- and NH_4^+ were determined on field campaigns D261 and FISHES following the incorporation of the stable isotope ^{15}N. Triplicate water samples from 6 depths within the euphotic zone were distributed into 640 mL clear polycarbonate bottles and ^{15}N–NO_3 and ^{15}N–NH_4 were added at a final concentration of 10% ambient NO_3^- and NH_4^+, except under oligotrophic conditions when the minimum addition was 5 nmol l^{-1} (Rees, Woodward, & Joint, 2006). Incubations were made in the same on-deck incubators used for the PP measurements for 24 h. Incubations were terminated by filtration (<40 cm Hg vacuum) onto ashed Whatman GF/F filters, which were dried onboard and stored over silica gel desiccant until they were returned to the laboratory. Particulate nitrogen concentration and ^{15}N atom% were determined by continuous flow stable isotope mass spectrometry using techniques described by Barrie and Lemley (1989) and Owens and Rees (1989). Rates of uptake were calculated according to Dugdale and Goering (1967) and when appropriate were corrected for over addition of ^{15}N tracer (Rees, Joint, & Donald, 1999).

Nitrification in the euphotic zone can make a variable contribution to the NO_3^- pool available to phytoplankton, which can therefore lead to an overestimate in f-ratio and subsequently estimates of new production (Yool et al., 2007). Nitrification rate measurements were not performed during these field programs and, therefore, derived new production should be considered to be at the upper range of the values. We have confidence that these are not anomalous as measurements during D261 were made during the early spring bloom period when NO_3^- is dominated by that derived from winter mixing and those during FISHES were at high latitude where the influence of nitrification on f-ratio estimates is likely to be minimal, in part due to the short growing season (Yool et al., 2007). NP was estimated from the product of net primary production and the f-ratio (Eppley & Peterson, 1979). NO_3^- is therefore considered to be "new" and NH_4^+ is considered as the regenerated nitrogen pool, so that the f-ratio was determined as follows:

$$\text{f-ratio} = NO_3\text{-uptake} / \left(NO_3\text{-uptake} + NH_4{}^+\text{uptake}\right) \quad (3)$$

2.5. Remote sensing algorithms of primary (PP) and new production (NP)

Two satellite models were used to estimate PP; the VGPM and WRM. Using PP from each model, NP was then computed using the model of Laws et al. (2000). The description of each model and parameterisation is given below. The VGPM was selected as it is the most cited PP algorithm currently used. It is empirical in nature and offers a simple approach to estimate PP by integrating over wavelength and depth (WIDI) in the water column using surface values as seen from satellite. This was compared against the WRM which is far more complex and computationally expensive as it resolves PP over both wavelength and depth (WRDR). Both WIDI and WRDR models have been compared in recent NASA round robin exercises (Carr et al., 2006; Friedrichs et al., 2009; Saba et al., 2011). To assess their accuracy, each model was run using both satellite and in situ data.

2.5.1. VGPM model of primary production (PP_{VGPM})

The model of Behrenfeld and Falkowski (1997) was driven by surface Chla. The euphotic depth (Z_{eu}) was computed from Chla following the relationships of Morel and Berthon (1989). The optimum photosynthetic rate (P_{opt}^B) was derived from SST using the seventh order polynomial of Behrenfeld and Falkowski (1997). PP_{VGPM} is calculated as follows:

$$PP_{VGPM} = 0.66125.P_{opt}^B [E_0/(E_0 + 4.1)] Z_{eu} C_{opt} D_{irr} \quad (4)$$

2.5.2. WRM of primary production (PP_{WRM})

The wavelength resolving model (WRM) of Morel (1991) was implemented following Smyth, Tilstone, and Groom (2005). The maximum quantum yield for growth (ϕ_m) and the maximum phytoplankton Chla-specific absorption coefficient (a^*_{max}) were parameterised using Chla following Morel, Antoine, Babin, and Dandonneau (1996). The above-water spectral light field was generated using the Gregg and Carder (1990) model run at 5 nm wavelength and 30 minute time resolution so that PP can be integrated over the day. Meteorological and ozone data to drive the model were obtained from National Centers for Environmental Prediction (NCEP) and Earth-Probe Total Ozone Mapping Spectrometer data (EPTOMS), respectively. Cloud fields were obtained from European Centre for Medium Range Weather Forecasts (ECMWF) model output and used to modify the above water light field following Reed (1977). The light field was propagated through the water column by calculating the spectral attenuation coefficient for downwelling irradiance following the methods of Morel (1988) as outlined in Tilstone, Smyth, Gowen, Martinez-Vicente, and Groom (2005). Hourly rates of PP were weighted to the water column light field and carbon fixation was integrated over the light hours for each day down to 1% irradiance depth. Integration was performed over all daylight hours, for wavelengths 400–700 nm and computed through the iterative approach of Morel and Berthon (1989). The model was run using surface Chla and temperature assuming a homogenous water column profile of Chla, a^*_{max} and ϕ_m, since this is what is available from satellite. PUR irradiance was estimated using Morel (1991) and PAR derived from the Gregg and Carder (1990) model. PP_{WRM} was calculated as follows:

$$\sum PP_{WRM} = 12\, a^*_{max}\, \phi_m \int_0^D \int_0^{z_{eu}} \int_{400}^{700} Chla(z) PUR(z,t,\lambda) f(x(z,t))\ d\lambda\ dz\ dt \quad (5)$$

2.5.3. Photosynthesis–temperature model of new production

Satellite estimates of NP were calculated from the model of Laws et al. (2000) from which the f-ratio was computed as a function of temperature and net photosynthesis (mg N m^{-3} d^{-1}). The look up table of

f-ratio, temperature and net photosynthesis was downloaded from the JGOFS web site and implemented in C^{++} to derive f-ratios from satellite values of Pathfinder Advanced High Resolution Radiometer (AVHRR) SST v2009 and PP from either the VGPM or WRM.

2.5.4. Satellite maps of primary and new production

Daily satellite images of PP and NP for match-up analysis were generated using 1 km data. Mean monthly satellite maps of PP and NP were generated using 9 km data. For each model, PP were generated from 1998 to 2010 using monthly NASA SeaWiFS OC4v6 Chla from the 2010 reprocessing (R2010) downloaded from the NASA Ocean Colour web site. AVHRR SST and PAR (Frouin & Pinker, 1995) for each province. The PAR monthly fields are average daily integrated values; downwelling irradiance values at each wavelength $E_d(\lambda)$ were retrieved using a look up table as described in Smyth et al. (2005). Each PP model was coupled to the NP model (Laws et al., 2000) to generate mean monthly maps of NP for the Irminger Sea from 1998 to 2010. Though we illustrate the variability in monthly mean PP and NP for 2010, these data were not used to calculate annual PP and NP due to the influence of the Icelandic volcano Eyjafjallajökull, which erupted during the summer of 2010 (Achterberg et al., 2013). SeaWiFS Chla 2010 values are likely to be erroneous for the Irminger Sea due to failure in the satellite atmospheric correction associated with volcanic particles (Porter, Kono, & Nielsen, 2005).

2.6. Statistical analyses and hydrographic zones

In situ data within ±3 h of satellite overpass were compared to the mean of a 3 × 3 pixel array around the sampling station following the procedures outlined in Bailey and Werdell (2006). Considering all six cruises, there were 14 satellite match-ups for PP and 5 for NP. The in situ and satellite data were compared using linear regression analysis and the following statistics to evaluate model performance: Mean (*M*) and standard deviation (*S*) of the $\log_{10}$-difference error between measured and satellite NP and PP and also the $\log_{10}$ root-mean square ($\log_{10}$-RMS) between measured and satellite NP and PP. We also used the inverse transformed ratio between satellite and measured values M (F_{med}), M − S (F_{min}) and M + S (F_{max}) following Campbell et al. (2002). The relative percentage difference (RPD) was calculated to illustrate the uncertainty between measured and satellite NP and PP. The distribution of PP and NP were transformed until no significant difference was found between the expected and the observed distributions using the Kolmogrov–Smirnov with Lilliefors test to ensure homoscedasticity (Sokal & Rolf, 1997). One-way analysis of variance (ANOVA) was also used to test whether there were significant differences between satellite and in situ estimates of NP and PP. The ANOVA results are given as $F_{1,df} = x$, $P = y$ where F is the mean square to mean square error ratio, the sub-script numbers denote the degrees of freedom and P is the ANOVA critical significance value.

We evaluated differences in mean monthly and annual PP and NP between satellite models in the six major hydrographic zones described in Section 2.1. Mean monthly and annual PP and NP were extracted for each model in each of these zones and differences between them were analysed by ANOVA. Monthly and annual PP and NP data were spatially integrated to achieve a single number per province. To assess differences between models over different temperature ranges, PP values were extracted at every 10 km along SW–NE transects from 60°N, 42.5°W to 65°N, 32.5°W in the EGC; 59°N, 40°W to 63°N, 31.5°W in the CIC; 56.5°N, 36°W to 63°N, 31°W in the SIC; 58.5°N, 33°W to 63°N, 25°W in the RKR; 55°N, 30°W to 61°N, 22.5°W in the ICB and along a SE–NW transect in the NIC from 63°N, 27.5°W to 65°N, 30°W (Fig. 1). PP_{VGPM} was then regressed against PP_{WRM} as a function of SST at 5°C increments from 0 to 15°C to assess the temperature dependency of each model.

For time series analyses, mean monthly primary production anomalies were calculated by subtracting from each monthly value the corresponding monthly average for the time series from 1998 to 2010. The cumulative sums method was applied to the anomalies to further decompose the signal to highlight major changes in monthly data values along the time-series (McQuatters-Gollop, Mee, Raitsos, & Shapiro, 2008). The average annual cumulative sum in anomalies of NP was compared against the cumulative sum in NAO, AO and MEI. The NAO monthly indices were taken from www.cgd.ucar.edu/cas/ which is based on the normalised sea level pressure difference between Ponta Delgada, Azores and Stykkisholmur Reykjavik. AO was downloaded from NOAA: www.cpc.ncep.noaa.gov/products/precip/CWlink/daily_ao_index/ao_index.html. AO is the difference in pressure between the Arctic and the northern middle latitudes and is calculated by projecting the monthly mean 1000 hPa height poleward of 20°N onto its first leading EOF mode. MEI was also downloaded from NOAA: www.esrl.noaa.gov/psd/enso/mei/. MEI is calculated as the first unrotated Principal Component from six variables: sea-level pressure, zonal and meridional components of the surface wind, sea surface temperature, surface air temperature, and total cloudiness fraction of the sky.

3. Results

3.1. Accuracy assessment of primary and new production satellite algorithms in the North Atlantic

The performance of the VGPM and WRM models was assessed using Chla and SST, from, firstly, in situ measurements (Fig. 2, Table 2) and, secondly, satellite estimates (Fig. 3B, C, Table 2) to calculate PP. PP_{WRM} had the lowest mean log-difference error in measured and satellite (M), standard deviation mean log-difference errors in measured and satellite (S), log-RMS and intercept, the highest r^2 and F_{med}, F_{max} and slope closest to 1 using both the in situ and satellite data (Table 2), indicating that PP_{WRM} was the most accurate model. There was no significant difference between in situ and modeled PP estimated from both in situ measurements of Chla and SST ($F_{1,165} = 1.58$, $P = 0.211$) and satellite data ($F_{1,27} = 0.202$, $P = 0.657$). The relative percentage difference (RPD) of PP_{WRM} compared to in situ PP was ~30% whereas the RPD of PP_{VGPM} was 80%. PP_{VGPM} had the highest M indicating a significant bias with a tendency to over-estimate PP, as indicated by the high F_{max} values. This increased the slope, intercept and log-RMS and resulted in a significant difference between in situ and PP_{VGPM} using both in situ ($F_{1,165} = 15.75$, $P < 0.001$) and satellite data ($F_{1,35} = 102.95$, $P = <0.001$) to estimate PP (Table 2). Using satellite data alone, PP_{WRM} was within 45% whereas the percentage difference between PP_{VGPM} and in situ values was higher.

Compared with in situ ^{15}N uptake, NP_{VGPM} explained 54% of the variance in in situ NP, whereas NP_{WRM} explained 73% of the variance (Fig. 2C, D). There was no difference between in situ NP and NP_{VGPM} ($F_{1,35} = 1.12$, $P = 0.297$), which were within 72% of the in situ values. There was also no difference between in situ NP and NP_{WRM} ($F_{1,35} = 0.002$, $P = 0.965$), which were within 10% of the in situ values. For NP_{WRM}, the slope, F_{med}, F_{max} and F_{min} were closer to 1 and the log-RMS error, *M* and *S* were lower compared to NP_{VGPM} (Table 2, Fig. 2C, D).

Fig. 3A gives in situ Chla versus SeaWiFS OC4v6 Chla at the stations sampled (Fig. 1) and corresponding validation statistics are given in Table 2. OC4v6 and in situ Chla were highly correlated having a high percentage variance explained, low bias, error, intercept, $\log_{10}$-RMS and UPD and a slope, F_{min}, F_{med} and F_{max} close to 1 (Table 2). Consequently, there was no significant difference between in situ and SeaWiFS OC4v6 Chla ($F_{1,27} = 0.002$, $P = 0.964$).

Using daily SeaWiFS data, there were only five in situ match-up stations for validating the NP models with satellite data (Fig. 3C), so a comprehensive validation was not possible. Similar to using in situ data, however, SeaWiFS derived NP_{WRM} was more accurate than NP_{VGPM} with a lower *M*, S and log-RMS, slope F_{med} and F_{max} closest to 1 (Table 2). There was no significant difference between in situ and NP_{WRM} ($F_{1,27} = 0.259$, $P = 0.625$) and the RPD was 11%. NP_{VGPM}

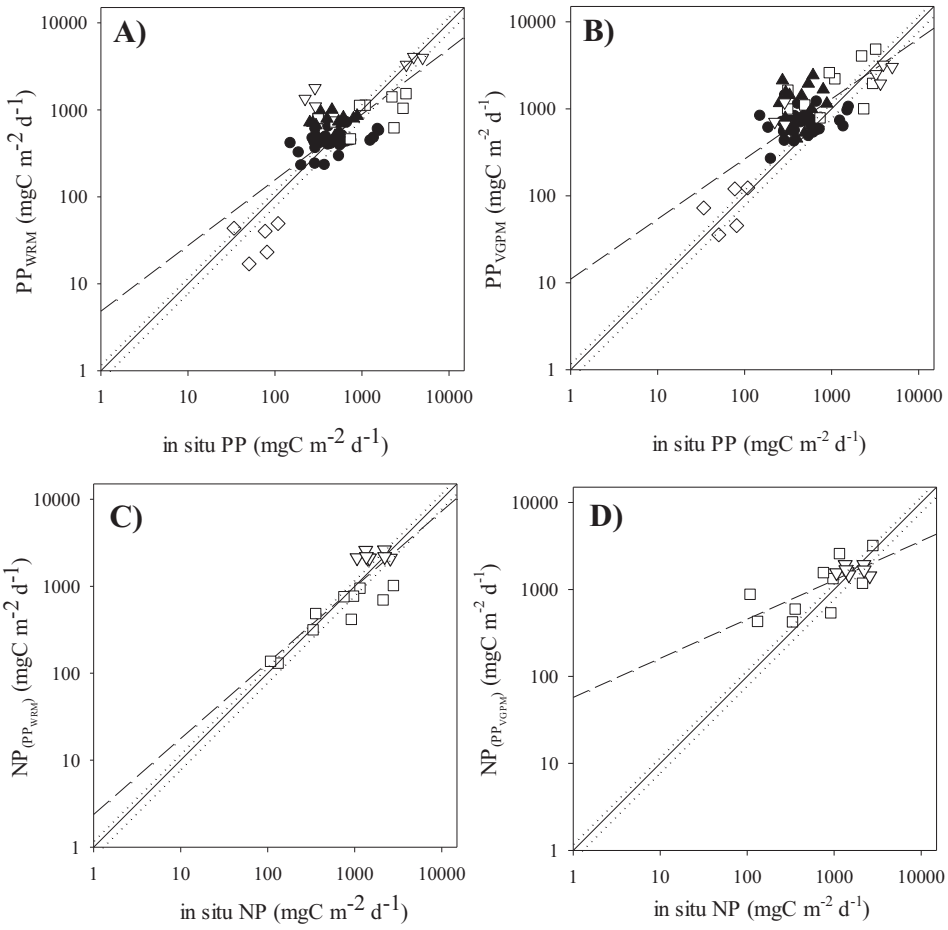

Fig. 2. Comparison of measured and modelled estimates of primary production (mg C m^{-2} d^{-1}) for the northern North Atlantic using in situ data to run the (A.) wavelength resolving model (WRM) of Morel (1991) (B.) VGPM of Behrenfeld and Falkowski (1997) and new production (mg C m^{-2} d^{-1}) estimated from Laws et al. (2000) for (C.) the WRM and (D.) the VGPM. Solid line is the 1:1 line, dotted lines are the 20% quartiles and dashed line is the regression. Filled circles are JC011 and JC037, open squares FISHES, filled triangles D264, open diamonds D267, inverted open triangles D261.

Table 2
Algorithm performance indices for new (NP) and primary production (PP) algorithm inter-comparison. Log-difference errors in measured and satellite estimates are given as Mean (*M*), Standard deviation (*S*) and root-mean square (Log RMS). The geometric mean and one-sigma range of the ratio (F = Value$_{alg}$/Value$_{meas}$) are given by F_{med}, F_{min}, and F_{max}, respectively; values closer to 1 are more accurate. *N* is the number of data used. Percentage variability explained (r^2), slope and intercept are for log–log regression. VGPM is vertical generalized production model; WRM is wavelength resolving model. The algorithm with the highest precision is highlighted. OC4v6 is the default SeaWiFS ocean colour algorithm for case 1 waters.

	M	S	*Log RMS*	*RPD*	F_{med}	F_{min}	F_{max}	r^2	*Inter cept*	*Slope*
SeaWiFS										
OC4v6	0.01	0.14	0.14	3	0.99	0.72	1.35	0.95	−0.01	0.85
N = 14										
In situ										
PP$_{(VGPM)}$	0.23	0.27	0.32	85	1.71	**0.93**	3.17	0.57	0.81	0.79
PP$_{(WRM)}$	**0.02**	**0.21**	**0.20**	**32**	**1.06**	0.66	**1.71**	**0.57**	**0.25**	**0.94**
N = 83										
NP$_{(VGPM)}$	0.12	0.29	0.32	72	1.32	**0.68**	2.56	0.54	1.76	0.45
NP$_{(WRM)}$	**0.01**	**0.23**	**0.23**	**10**	**0.99**	0.59	**1.66**	**0.73**	**0.38**	**0.87**
N = 18										
SeaWiFS										
PP$_{(VGPM)}$	1.31	0.56	1.53	3591	20.47	5.61	74.63	0.30	4.71	−0.20
PP$_{(WRM)}$	**0.06**	**0.34**	**0.36**	**45**	**1.14**	**0.52**	**2.53**	**0.54**	**2.06**	**0.29**
N = 14										
NP$_{(VGPM)}$	0.95	0.67	1.45	2763	8.88	1.90	41.51	**0.77**	4.88	−0.33
NP$_{(WRM)}$	**0.14**	**0.31**	**0.40**	**−11**	**0.72**	**0.35**	**1.49**	0.61	**1.12**	**0.57**
N = 5										

exhibited a negative regression caused by an over-estimation at low values, which resulted in disproportionately high F_{med}, M and log-RMS and a significant difference between in situ and NP$_{VGPM}$ ($F_{1,27}$ = 15.92, P = 0.004) (Fig. 3C) and very high RPD (Table 2).

3.2. Satellite estimates of new and primary production for the northern North Atlantic

Mean monthly PP and NP images generated from the two models for April, June and August from 1998 to 2010 of the Irminger Sea are given in Figs. 4 and 5, respectively. The corresponding mean monthly time series for each hydrographic province are given in Figs. 6 and 7. Both models exhibited the same temporal pattern, with an increase in PP and NP from April to June, followed by a decrease in August. They also showed the same spatial patterns, with higher values in the EGC, ICB and RKR and lower values in the CIC, NIC and SIC. PP$_{VGPM}$ and NP$_{VGPM}$ consistently had significantly higher values than PP$_{WRM}$ and NP$_{WRM}$ (Table 3). Over all zones, PP$_{VGPM}$ was 1.4 times higher compared to PP$_{WRM}$ and NP$_{VGPM}$ was 2.07 times higher than NP$_{WRM}$ (Table 3). PP$_{VGPM}$ was 1.54 times higher in the spring and 1.28 times higher during summer and winter. The models showed better agreement in the autumn when PP$_{VGPM}$ was only 1.02 times higher than PP$_{WRM}$. The differences between models varied by province and were greatest in the ICB by a factor of 1.45, and closest in EGC where there was a factor of 1.31 difference (Figs. 4, 6). The inter-annual variability also changed between models and hydrographic zones (Figs. 4, 6). For PP$_{WRM}$ and NP$_{WRM}$ in

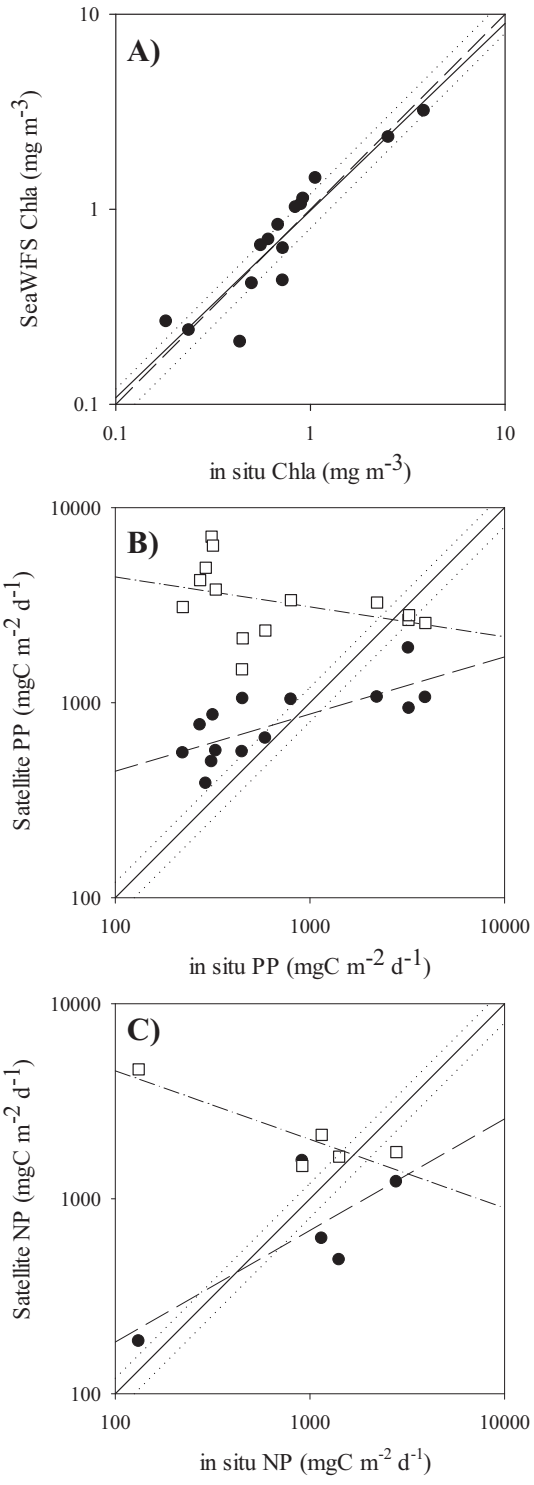

Fig. 3. Comparison of measured and satellite estimates of (A.) SeaWiFS Chla (mg m^{-3}), (B.) primary production, mg C m^{-2} d^{-1} and (C.) new production, mg C m^{-2} d^{-1} for the northern North Atlantic using satellite data to run the satellite models. VGPM is open squares, WRM is filled circles, Solid line is the 1:1 line, dotted lines are the 20% quartiles and dashed line is the regression. Symbols in (B.) and (C.) as in Fig. 2.

the NIC, SIC, CIC and RR, the highest PP and NP occurred in summer 2010 followed by spring 2008 and the lowest values in spring 2005 (Figs. 4, 5, 6, 7). In the ICB, the highest PP_{WRM} and NP_{WRM} occurred in 2010 and the lowest were an order of magnitude lower in 2005. For PP_{VGPM} and NP_{VGPM} in the CIC, NIC, SIC, RKR and ICB, the highest PP and NP also occurred in summer 2010 and the lowest values in spring 2002. High spring values also occurred from 2006 to 2009 in the EGC, RKR and ICB. Mean annual satellite estimates of PP and NP are given in Tables 4 and 5. Both models had the highest annual PP in the ICB and lowest in the CIC (Table 4). For NP, both models exhibited the lowest values in the CIC. The highest mean annual NP_{VGPM} values were in the ICB, whereas NP_{WRM} was slightly higher in the RKR (Table 5).

3.3. Climate forcing and primary production in the northern North Atlantic

The average annual cumulative sum of the anomalies in NP_{VGPM}, and NP_{WRM} were compared in the six hydrographic zones (Fig. 8). For these cumulative sums in NP_{VGPM} and NP_{WRM}, the trend was similar in all provinces and for both models, with a gradual decrease from 1998 to 2009, followed by an increase to 2010. The magnitude of the decrease was greater for NP_{VGPM} compared to NP_{WRM} in the ICB, NIC and CIC, which was on average 9.3, 1.3 and 1.1 times higher, respectively. In the ICB, the NP_{VGPM} showed an initial rise in cumulative sums until 2000, whereas the NP_{WRM} decreased until 2000. In the SIC, the decrease in cumulative sums was greater for NP_{WRM} compared to NP_{VGPM}. By contrast, in the EGC, there was little difference in cumulative sums between both models. The cumulative sums of the anomalies in NP for each model were then correlated against those for NAO, AO and MEI (Table 6). The mean cumulative sum of the anomalies in NAO increased slightly from 1998 to 2000 and then gradually decreased until 2006, when there was a slight increase to 2007 followed by a decrease to 2010. NP_{WRM} exhibited a significant positive correlation with NAO in the EGC and CIC. NP_{VGPM} also showed a significant positive correlation with NAO in the EGC and CIC and additionally in the SIC.

Both NP_{VGPM} and NP_{WRM} showed significant negative correlations with the cumulative sum in AO, which was consistently higher in the EGC and CIC compared to the other hydrographic zones (Table 6). The AO changed from negative in 1998 to positive from 1999 to 2009. The response to this positive phase and especially in EGC and CIC, was a consistent decrease in the mean cumulative sum of the anomalies in NP_{VGPM} and NP_{WRM}. From 2009 to 2010 there was a reduction in mean cumulative sum of the anomalies in AO, which was paralleled by a decrease in those for NP.

NP_{VGPM} exhibited a significant negative correlation with MEI in the ICB. There was an initial increase in NP_{VGPM} In the ICB from 1998 to 2000 as MEI switched from positive to negative, followed by a decrease in NP_{VGPM} from 2000 to 2007 as MEI switched from negative to positive (Fig. 8).

4. Discussion

4.1. Validation of satellite algorithms of new and primary production in the northern North Atlantic

There has been much debate on the global applicability of satellite models since some areas exhibit atypical optical (Dierssen & Smith, 2000; Volpe et al., 2007) or photo-physiological characteristics (Sathyendranath, 2000). A comprehensive knowledge of the extent to which these vary, both spatially and temporally, is required so that global models can be fine-tuned to regional conditions. Even at local scales, the optical properties of the world's oceans are changing (Dierssen, 2010) and on-going validation of ocean colour algorithms is therefore necessary to continually monitor their accuracy. The northern North Atlantic is typified by low solar zenith angles during winter and long day length during summer, which can cause a high variation in phytoplankton photo-physiology (Moore, Lucas, Sanders, & Davidson, 2005). PP_{WRM} and NP_{WRM} were more accurate than PP_{VGPM} and NP_{VGPM} using both in situ and satellite data (Table 2). Campbell et al. (2002) assessed the performance of 12 satellite algorithms forced with in situ data, against 89 ^{14}C measurements. WRMs, WIDIs such as the VGPM and time-independent models (TIM) showed a similar performance. Each model however, exhibited a regional dependency. In their study in the North Atlantic, data were available from only 20 stations and WRM and TIM types

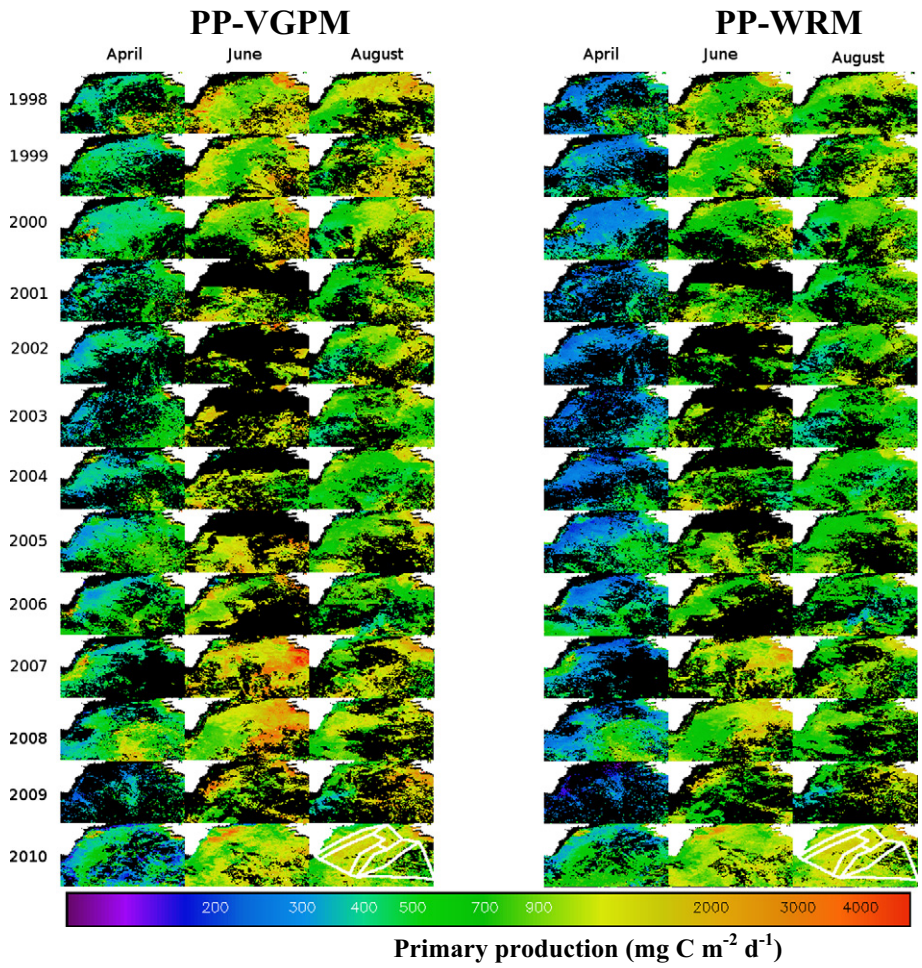

Fig. 4. Mean monthly satellite maps of primary production (mg C m^{-2} d^{-1}) for the northern North Atlantic in April, June and August from 1998 to 2010 using the VGPM (left hand panel) and WRM (right hand panel). Hydrographic zones are illustrated in the bottom right hand image of each panel; for description of the zones refer to Fig. 1.

were more accurate. Carr et al. (2006) compared 24 satellite and ecological models forced with mean monthly satellite data. The WRM and DIM models proved to be closest to the mean of all 24 models, especially in the Atlantic. There was however no in situ PP data to perform a comprehensive model validation. Tilstone, Smyth, Poulton, and Hutson (2009) compared PP models in the Atlantic Ocean and found that a WRM was more accurate than VGPM in six out of nine Atlantic Ocean biogeographic provinces. Saba et al. (2010) compared 36 models at Bermuda Atlantic Time series Study (BATS) and the Hawaii Ocean Time series (HOT) using nearly two decades of in situ data. At both these sites the average bias of the biogeochemical ocean circulation models (BOGCMs) was almost twice that of the ocean colour models. Saba et al. (2011) then compared 36 models including 22 ocean colour models and 14 BOGCMs against a large in situ dataset of ^{14}C (N = 1156) and found that the average uncertainty across all models was 31% and WRM type models proved to be most accurate in eight out of ten regions. Similarly, we found for the North Atlantic that PP_{VGPM} was 85% higher than in situ PP, whereas PP_{WRM} was within 30%. This varied between hydrographic zones and was highest in the ICB and lowest in the EGC (Fig. 4, Table 2). For NP, VGPM was 72% higher than in situ data whereas for the WRM the difference was only 10% (Fig. 5). Using the models with SeaWiFS data, differences were greatest in the ICB and lowest in the EGC (Fig. 6, Table 4), however there were only a limited number of satellite match-ups (N = 5) with in situ NP. Measurements of NP are rare and there is an obvious need for more in situ measurements of NP to improve both remote sensing and ecosystem models and in turn to enhance our understanding of both food web dynamics and carbon cycling.

4.2. Causes of differences between satellite algorithms of new and primary production in the North Atlantic

To assess reasons for differences in model performance, we used sensitivity analyses to ascertain which of the input parameters produced the greatest error in PP estimates from the two models. Each variable used to compute PP was fixed at its mean and PP was then re-computed by varying the parameter through its observed maximum and minimum. The results are summarised as box plots in Fig. 9. The total mean error given below each plot, indicates the degree a variable influences the computation of PP; the higher the error, the greater the influence. For PP_{VGPM}, C_{insitu} and Z_{eu} had the greatest influence while for PP_{WRM}, C_{insitu} and ϕ_m exhibited the greatest effect. In both models, Z_{eu} and ϕ_m are derived from C_{insitu}, which accounts for the high error in the computation of PP. That there was no significant difference between in situ and SeaWiFS Chla (Fig. 3, Table 2), suggests that the principal source of differences between models was not due to Chla. For the VGPM, plotting modeled Z_{eu} against in situ Z_{eu} derived from CTD profiles of PAR (Fig. 9C), illustrated a tendency for the VGPM to overestimate Z_{eu} especially in low Chla waters (diamonds in Fig. 9C). The percentage difference between measured and modeled Z_{eu} was 22% for the in situ stations. Behrenfeld and Falkowski (1997) concluded that their estimation of Z_{eu} would contribute to <15% of the error in the VGPM. The over-estimation of Z_{eu} may partially explain why PP_{VGPM} consistently resulted in higher values compared to PP_{WRM}, especially at the lower range of PP (Figs. 3B, 6B, C, D). Similarly, Saba et al. (2011) found the depth of the water column to be the main parameter limiting

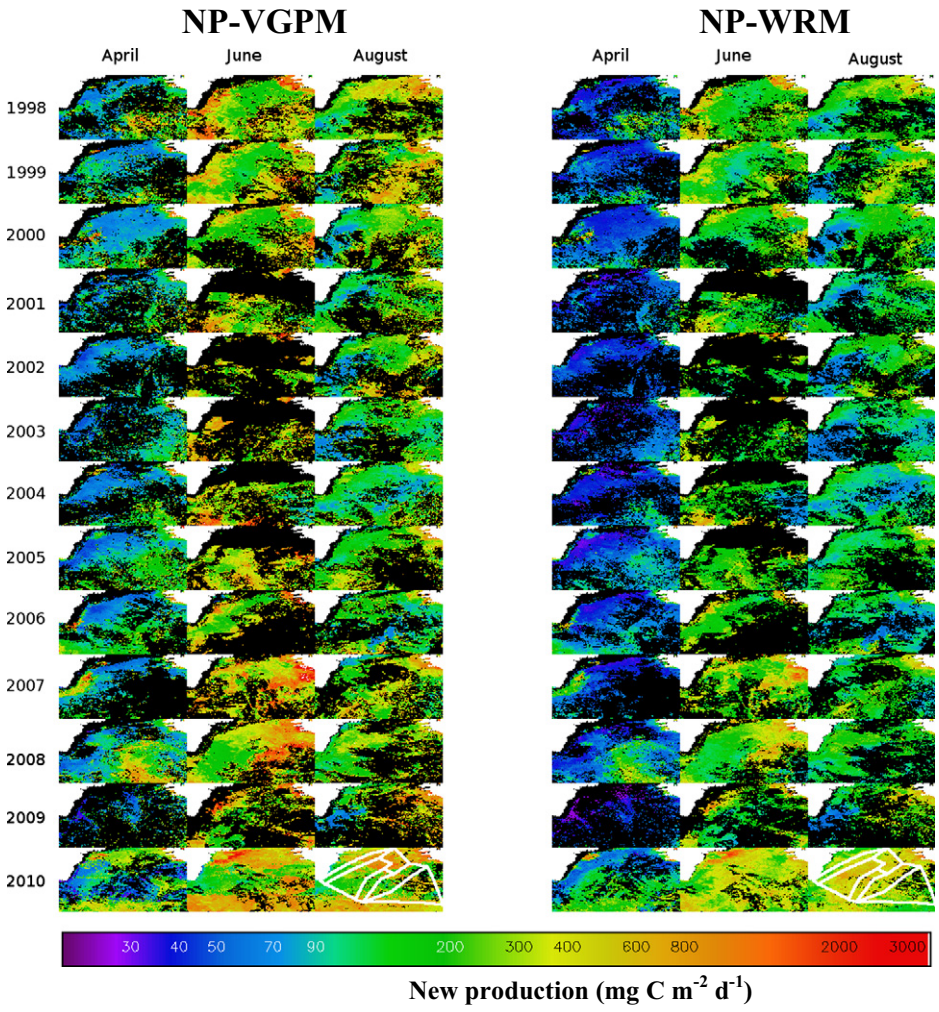

Fig. 5. Mean monthly satellite maps of new production (mg C m^{-2} d^{-1}) for the northern North Atlantic in April, June and August from 1998 to 2010 using the VGPM coupled with the new production model of Laws et al. (2000) (left hand panel) and WRM coupled with the Laws et al. (2000) model (right hand panel). Hydrographic zones are illustrated in the bottom right hand image of each panel; for description of the zones refer to Fig. 1.

the performance of most PP models. They observed that there was a tendency for the VGPM to under-estimate PP at bottom depths < 750 m and over-estimate PP at bottom depths > 4000 m due to errors in the simulation of Z_{eu}. Siegel et al. (2001) also found that the bias in the VGPM, when compared to a global in situ PP dataset, was more pronounced (−38%) when Chla concentration was low, and therefore Z_{eu} was deep. An under-estimate in Chla would lead to an over-estimate in Z_{eu} and higher PP values at low in situ values, which we also observed (Figs. 2B, 3B).

Carr et al. (2006) concluded from the PPARR3 inter-comparison that a better parameterisation of photo-physiology is required to improve model skill and accuracy. More recently, a comprehensive error analysis of the uncertainties associated with the VGPM also concluded that the largest individual contributor to the random uncertainty in PP was the input term that describes the physiological state of phytoplankton and changes in the rate of Chla-normalised photosynthesis over depth (Milutinovic & Bertino, 2011). Both the WRM and VGPM use SST to derive the photo-physiological term. We therefore assessed the temperature sensitivity of the photo-physiological term in each model by varying SST through the range in in situ values at each of the 83 stations sampled, whilst keeping Chla and PAR constant. P_b^{opt} and ϕ_m were then computed at 1 °C increments to estimate PP_{VGPM} and PP_{WRM} over the natural range in SST (Fig. 10). Both models exhibited a sigmoidal dependence to SST, with low sensitivity of PP over the temperature range 5 to 9 °C, when PP_{VGPM} was 15% higher than PP_{WRM}. Both models exhibited a sharp increment in PP from 9 to 10 °C, which was similar from 10–18 °C. Over this temperature range PP_{VGPM} was 40% higher than PP_{WRM}. Milutinovic and Bertino (2011) found that only 9% of the variability in P_b^{opt} could be described by the polynomial function of SST, indicating that temperature alone is a poor predictor of photosynthetic rates. This is further compounded by the depth dependency of P_b^{opt} with irradiance, which is not well characterised in the VGPM. When we plot PP_{WRM} against PP_{VGPM} from data extracted every 10 km along S–N transects (shown in Fig. 1) in the six hydrographic zones (Fig. 11) and as a function of temperature; from 0 to 5 °C, PP_{VGPM} was 43% higher than PP_{WRM}; from 5 to 10 °C PP_{VGPM} was 29% higher and from 10 to 15 °C PP_{VGPM} was 27% higher. Over the entire SST range, PP_{VGPM} was 35% higher than PP_{WRM}, which illustrates the temperature dependency of each of the models in this region. The differences between the models in each hydrographic zone are related to the temperature range that was encountered in each zone. For example, differences were greatest in the ICB where the temperature range was between 8 and 18 °C and lowest in the EGC where the temperature range was 5.5–15 °C. This is reflected in the sensitivity analysis which indicated that from 5 to 9 °C there will be a 15% difference between PP_{VGPM} and PP_{WRM}, whereas from 10 to 18 °C, the difference between models was greater (Fig. 10).

The dependency of P_b^{opt} is also determined by changes in irradiance and nutrients; however, these other variables often co-vary with temperature, which makes SST a convenient parameter to model changes in photosynthetic rates (Babin et al., 1991; Behrenfeld & Falkowski,

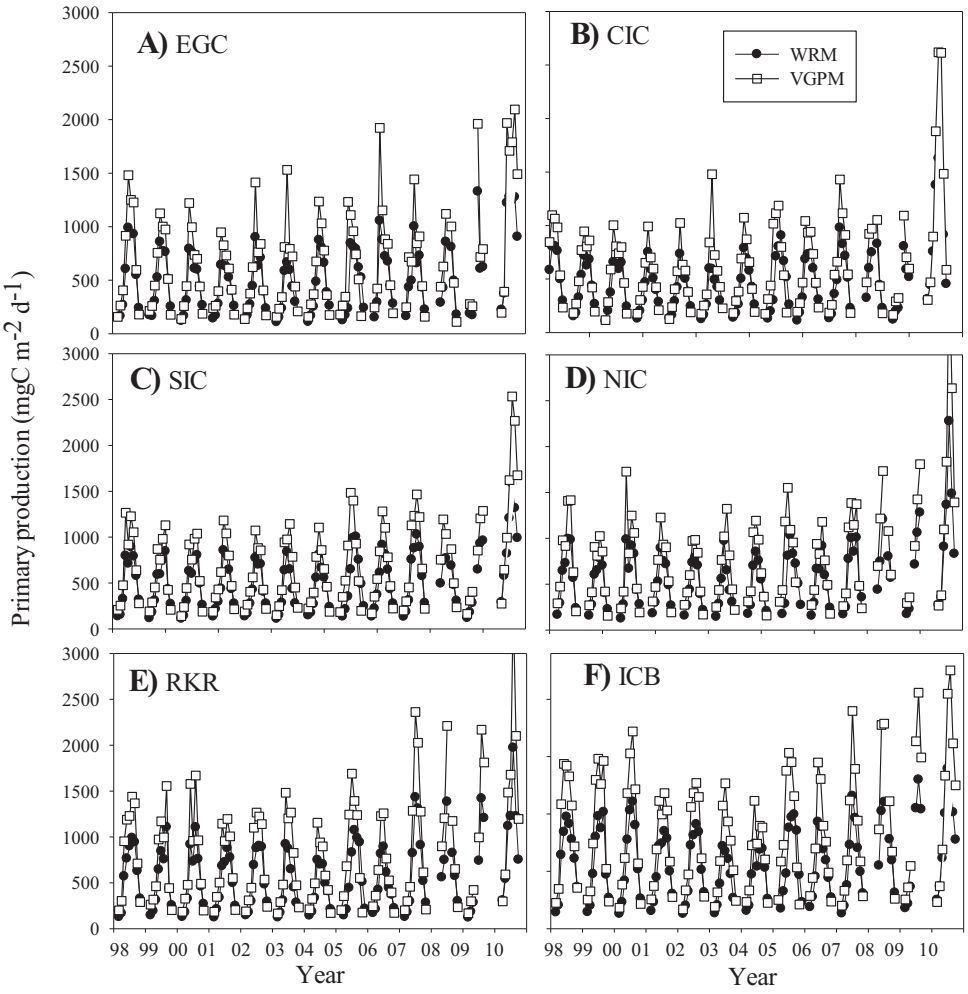

Fig. 6. Mean monthly variation in primary production using the WRM (filled circles) and the VGPM (open squares) from 1997 to 2010 in (A.) East Greenland Shelf (EGC), (B.) Central Irminger Sea (CIC), (C.) North Irminger Current (NIC), (D.) South Irminger Current (SIC), (E.) Reykajnes Ridge (RKR) and (F.) Iceland Basin (ICB).

1997), especially since SST can be sensed remotely at the same spatial and temporal scales as ocean colour. In the North Atlantic over the Scotian Shelf for example, 65% of the variation in the chlorophyll-normalised maximum photosynthetic rate (P^B_m) can be described by temperature alone (Bouman et al., 2003). Below 20 °C, increasing temperature results in an increase in P^B_m due to linear reaction kinetics (Raven & Geider, 1988). There are situations where temperature cannot account for changes in light and nutrients due to a decoupling between these parameters. For example, in warm, permanently stratified regions of the North Atlantic (typically in summer), where light is non-limiting, the P^{opt}_b dependency with SST does not account for the nutrient limitation that can occur. By contrast, in cool, well mixed environments, such as the northern North Atlantic during winter and spring when nutrients are replete, the depth dependency of P^{opt}_b with irradiance can become limiting. Under such conditions, P^{opt}_b has poor predictive capabilities of the photosynthetic rate and the uncertainty associated with the VGPM estimate of PP becomes large (Milutinovic & Bertino, 2011). Subsequently, a number of approaches to estimate changes in photo-physiology as a function of nutrient concentration or status have been proposed (Behrenfeld, Boss, Siegel, & Shea, 2005; Behrenfeld, Maranon, Siegel, & Hooker, 2002). These models are based on assumptions about ambient nutrient fields that are not available from remote sensing data. In addition, the correlation between dissolved inorganic nitrogen (DIN) and phytoplankton biomass or photosynthetic rates is often poor, because in winter when DIN is high, phytoplankton photosynthesis can be low due to light limitation. There can also be a lag response between a new supply of DIN and photosynthetic rate and once photosynthesis reaches a maximum at the peak of the bloom, DIN has been taken up by phytoplankton, which again results in a poor correlation between ambient DIN and photosynthetic rates (Maranon, Cermeno, Latasa, & Tadonleke, 2012). In view of these limitations, and since the kinetics of photosynthesis are tightly coupled to temperature especially over the range from 5 to 20 °C, selection of the most accurate model that uses an SST function to describe photo-physiology is a priority for accurate estimation of both PP and NP. Some new approaches to the parameterisation of P^B_m as a function of SST have recently become available (Saux-Picart, Sathyendranath, Dowell, Moore, & Platt, 2014) and warrant further validation to find the most accurate PP and NP models for both global and regional seas. Although both the VGPM and WRM use SST to describe changes in photosynthetic rates, we observed that variations in SST had a greater effect on P^{opt}_b in the VGPM than they did on ϕ_m in the WRM.

Behrenfeld and Falkowski (1997) argued that variability in PAR and its capacity to influence the relative depth of light saturation has a small impact on the resulting PP. Milutinovic and Bertino (2011) found that the PAR function used in the VGPM can result in large uncertainty (~12%) in PP. By comparison, the WRM incorporates a spectral-irradiance dependence of ϕ_m, which varies over depth as irradiance becomes attenuated and over time, as irradiance decreases either side of zenith. Despite the shortcomings of SST in describing variations in photo-physiology, the parameterisation of ϕ_m in the WRM formulated over two decades ago (Morel, 1991), provides more accurate estimation

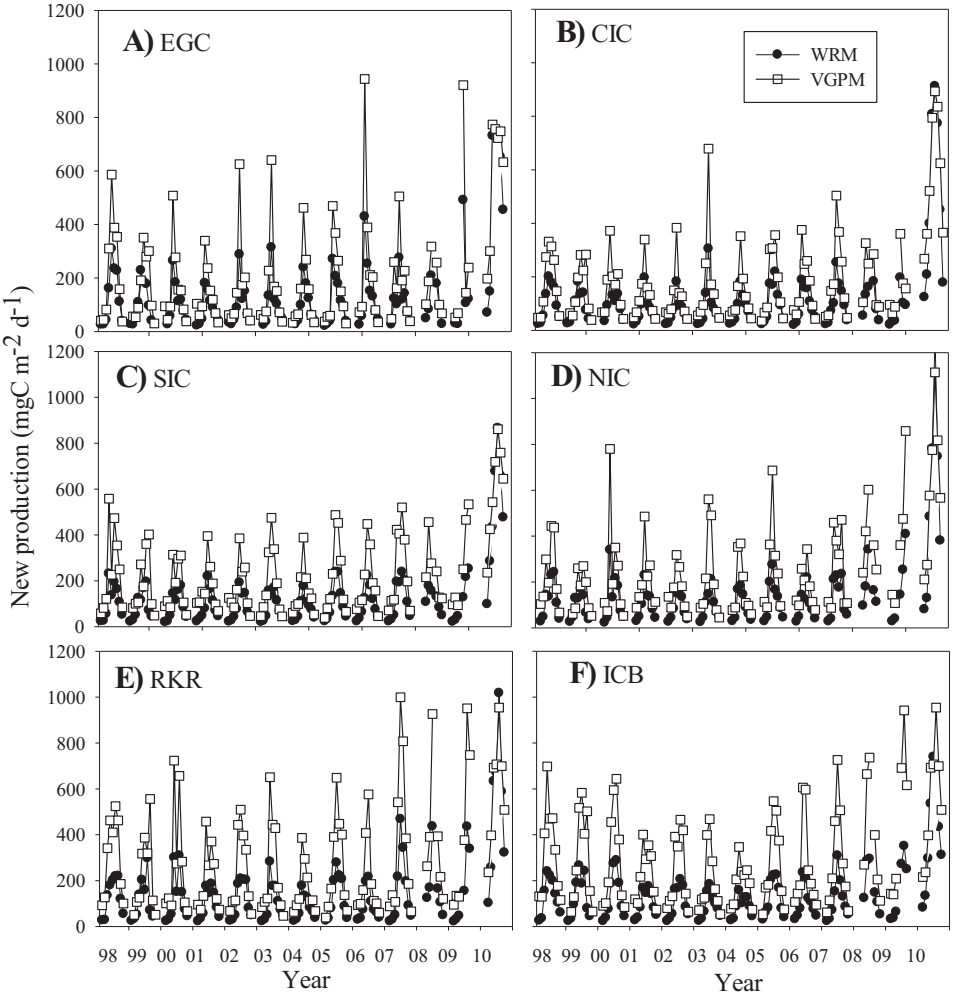

Fig. 7. Mean monthly variation in new production using the WRM (filled circles) and the VGPM (open squares) from 1997 to 2010 in (A.) East Greenland Shelf (EGC), (B.) Central Irminger Sea (CIC), (C.) North Irminger Current (NIC), (D.) South Irminger Current (SIC), (E.) Reykajnes Ridge (RKR) and (F.) Iceland Basin (ICB).

of PP and NP compared to the VGPM. On a global basis, Milutinovic and Bertino (2011) found that the systematic positive errors in P_b^{opt} in the VGPM contributed to a 6% bias in each pixel. The accumulated error from individual pixels for 2005, led to an overestimate of 2.5 Pg C of the 46.1 Pg C annual global PP. We found that there was a 28% difference in PP between the VGPM and WRM in 2005, which corresponded to a difference of 76 gC m^{-2} yr^{-1} for the northern North Atlantic alone. These differences in PP between models propagated to differences of ~50% in NP estimates for the northern North Atlantic.

Table 3
One Way Analysis of variance between VGPM-derived and WRM-derived differences in primary (PP) and new (NP) production. VGPM is vertical generalized production model; WRM is wavelength resolving model. F is the mean square to mean square error ratio and P is the ANOVA critical significance value. Level of significance to P = 0.05 is indicated; * is 0.05–0.01, **0.01–0.001, *** is <0.0001. EGC—Eastern Greenland Current; NIC—North Irminger Current; SIC—South Irminger Current; CIC—Central Irminger Sea; RKR—Reykajnes Ridge; ICB—Iceland Basin.

Province		*N*	F	P	Mean VGPM ($mgCm^{-2}d^{-1}$)	Mean WRM ($mgCm^{-2}d^{-1}$)
EGC	PP	217	4.75	0.0300*	627 ± 417	482 ± 275
	NP	214	8.65	0.0040**	182 ± 179	113 ± 92
CIC	PP	223	6.07	0.0140*	571 ± 331	445 ± 228
	NP	223	20.42	<0.0001***	158 ± 118	92 ± 61
NIC	PP	196	7.38	0.0070**	732 ± 428	545 ± 293
	NP	196	30.91	<0.0001***	227 ± 170	115 ± 82
SIC	PP	223	7.48	0.0070**	637 ± 377	484 ± 265
	NP	223	40.32	<0.0001***	199 ± 137	98 ± 66
RKR	PP	223	8.51	0.0040**	776 ± 536	552 ± 341
ICB	NP	223	38.08	<0.0001***	266 ± 223	123 ± 101
	PP	225	12.05	0.0010**	810 ± 486	566 ± 304
	NP	225	57.96	<0.0001***	281 ± 200	120 ± 81

4.3. Intra- and inter-annual variability in new and primary production in the Irminger Basin in different hydrographic zones

NP and the f-ratio are important components of food web dynamics and carbon cycling. There are limited in situ measurements of NP available however, and especially in the North Atlantic. Based on in situ measurements, previous studies in the Greenland Sea showed that new production during a *Phaeocystis* sp. bloom can reach 1100 mgC m^{-2} d^{-1} (Smith et al., 1991). Anderson, (2000) reported NP up to 5700 mgC m^{-2} d^{-1} for the Greenland Sea. From the in situ data we collected, NP varied from 100 to 2800 mgC m^{-2} d^{-1} in the Iceland Basin and 1000 to 2600 gC m^{-2} d^{-1} in the Celtic Sea. Based on changes in in situ N, Sanders et al. (2005) reported 36 gC m^{-2} yr^{-1} in the Irminger Basin in 2002. Annual new production based on temperature–nitrate relationships and Argo float data or silicate uptake has been predicted to be 65 gC m^{-2} yr^{-1} in 2002 (Henson et al., 2003, 2006). By comparison, in this study the mean NP_{WRM} from 1998–2009 over all hydrographic zones was ~41 gC m^{-2} yr^{-1}. From satellite data with an empirical algorithm, NP in the Irminger basin had previously been reported to be between 100–150 gC m^{-2} yr^{-1} (Falkowski, 1988; Laws

Table 4
Mean annual satellite estimates of primary production (PP) gC m^{-2} yr^{-1} for different biozones in the Irminger Basin. VGPM is vertical generalized production model; WRM is wavelength resolving model. EGC—Eastern Greenland Current; NIC—North Irminger Current; SIC—South Irminger Current; CIC—Central Irminger Sea; RKR—Reykajnes Ridge; ICB—Iceland Basin, TOTAL is the spatial average of all zones.

Year	Model	EGC	CIC	NIC	SIC	RKR	ICB	TOTAL
98	WRM	196	178	210	190	219	222	203
98	VGPM	263	230	288	256	311	324	279
99	WRM	175	159	173	165	190	212	179
99	VGPM	222	200	221	215	259	308	237
00	WRM	165	159	206	166	197	218	185
00	VGPM	208	202	281	212	278	309	248
01	WRM	158	147	188	166	181	192	171
01	VGPM	187	182	243	214	247	264	223
02	WRM	158	138	169	156	193	194	168
02	VGPM	201	168	213	217	261	265	218
03	WRM	140	135	174	154	172	158	156
03	VGPM	212	205	241	217	260	239	229
04	WRM	162	155	176	156	159	174	164
04	VGPM	205	193	234	201	211	234	213
05	WRM	177	182	211	196	217	218	200
05	VGPM	223	234	315	263	306	318	276
06	WRM	205	182	183	179	169	192	182
06	VGPM	279	214	232	234	227	266	242
07	WRM	189	179	222	204	238	205	206
07	VGPM	248	236	292	279	354	298	185
08	WRM	203	206	290	219	286	277	247
08	VGPM	252	263	410	289	421	413	341
09	WRM	223	155	239	187	233	253	215
09	VGPM	311	202	331	253	343	388	305

et al., 2000). By comparison, using the WRM we found NP to vary between 26 gC m^{-2} yr^{-1} in the CIC in 2002 to 70 gC m^{-2} yr^{-1} in the RKR in 2008, which is the upper limit reported for the seasonally stratified NW European Shelf (Heath & Beare, 2008). By comparison, for the northern North Atlantic NP_{VGPM} was between 45 and 166 gC m^{-2} yr^{-1}.

Biological production in the Irminger Basin can often be limited by silicate (Allen et al., 2005; Sanders et al., 2005), which becomes depleted in late spring potentially leading to a limitation of diatom growth (Henson et al., 2006). These studies suggest that a nutrient proxy for photosynthesis would best describe PP and NP. The estimates of NP by

Table 5
Mean annual satellite estimates of new production (NP) gC m^{-2} yr^{-1} for different biozones in the Irminger Basin. VGPM is vertical generalized production model; WRM is wavelength resolving model. EGC—Eastern Greenland Current; NIC—North Irminger Current; SIC—South Irminger Current; CIC—Central Irminger Sea; RKR—Reykajnes Ridge; ICB—Iceland Basin, TOTAL—all regions combined.

Year	Model	EGC	CIC	NIC	SIC	RKR	ICB	TOTAL
98	WRM	48	37	44	40	48	48	44
98	VGPM	81	64	85	90	110	119	91
99	WRM	38	32	34	33	41	47	38
99	VGPM	59	54	55	67	82	108	71
00	WRM	40	37	48	33	46	49	42
00	VGPM	59	64	88	63	98	109	79
01	WRM	30	28	37	32	36	37	34
01	VGPM	49	47	73	62	76	82	65
02	WRM	35	26	32	31	42	39	34
02	VGPM	58	45	60	61	88	87	67
03	WRM	39	34	35	32	32	33	35
03	VGPM	60	64	81	70	87	73	72
04	WRM	37	29	34	32	30	32	32
04	VGPM	53	47	63	56	59	69	58
05	WRM	40	38	45	41	48	45	43
05	VGPM	62	61	99	76	97	100	83
06	WRM	53	34	36	36	34	39	39
06	VGPM	93	59	64	70	73	93	75
07	WRM	41	34	48	44	59	43	45
07	VGPM	69	59	93	93	135	105	94
08	WRM	44	43	70	44	70	64	56
08	VGPM	69	70	64	70	73	93	114
09	WRM	63	43	59	41	59	61	52
09	VGPM	117	61	133	91	140	166	118

Henson et al. (2006) used the VGPM, but constrained the model using $Si(OH)_4$ limitation in the region and their results (~65 gC m^{-2} yr^{-1}) were lower than those of Falkowski, Barber, and Smetacek (1998) and Laws et al. (2000). More recently, Henson et al. (2011) developed a model of export production using a large database of thorium (^{234}Th) derived export measurements, which they extrapolated globally through correlations between PP and SST, and from this, estimated global integrated carbon export to be 5 GtC yr^{-1} lower than previous estimates, which is 60% lower than the e/f-ratio based estimate. The PP input used in the Henson et al. (2011) model was from three algorithms (Behrenfeld & Falkowski, 1997; Carr, 2002; Marra, Trees, & O'Reilly, 2007). Based on our study, if PP_{WRM} were used as input to the Henson et al. (2011) model, the resulting export production would be 7–8 GtC yr^{-1} lower. Our results suggest that the PP model used as input to either new or export production model is critical in computation of these parameters.

4.4. Variability in new production as a function of climate indices

Predicted changes in temperature, stratification and nutrient input can affect the f-ratio and thus impact upper trophic levels and carbon export. Saba et al. (2010) found that between 1989 and 2007 in situ PP at BATS and HOT increased by an average of nearly 2% per year, which at the BATS site was forced by more frequent mixing events during negative NAO phases. They found that none of the satellite models tested could reproduce this change over time. Over the past 30 years, there have been major fluctuations in atmospheric forcing in the northern North Atlantic which is reflected in the NAO (Hakkinen & Rhines, 2004). Positive NAO results in a later spring bloom in North Atlantic sub-polar waters (Henson, Dunne, & Sarmiento, 2009). A large positive NAO index is usually associated with strong westerly winds and low pressure around Iceland (Hurrell & Deser, 2009). Bentsen, Drange, Furevik, and Zhou (2004) observed that convective mixing in the Labrador and Irminger Seas is linked to the NAO such that negative NAO leads to deeper vertical mixing in these regions. This may suggest that negative NAO in winter results in deeper convective mixing, which could enhance the supply of nutrients to the photic zone for the onset of the spring bloom and thus affect the magnitude of the annual new production. Herein, NP_{WRM} and NP_{VGPM} were positively correlated with NAO in the EGC and CIC. In addition, NP_{VGPM} was also correlated with NAO in the SIC. During the SeaWiFS time series from 1997–2000, there was an intense reversal of the winter NAO index (Hakkinen & Rhines, 2004), which caused an initial increase in the average annual cumulative sum of the anomalies in NAO and a decrease in those of NP (Fig. 8). From 2001–2005 the NAO then fluctuated between weak positive and negative (Hakkinen & Rhines, 2009), which lead to a decrease in the average annual cumulative sum of the anomalies in NAO and NP. After 2006, the NAO switched to positive and the average annual cumulative sum of the anomalies increased, whereas those for NP continued to decrease in parallel with further decrease in NAO from 2007 to 2009. From 2009 to 2010 the average annual cumulative sum of the anomaly in NP increased, though this could be due to the summer 2010 eruption of the Icelandic volcano Eyjafjallajökull (Achterberg et al., 2013). Volcanic particles are known to cause failure in satellite atmospheric correction, and in turn could cause anomalies in ocean colour which may have caused increases in annual NP values. Zhai, Platt, Tang, Sathyendranath, and Walne (2013) observed two competing mechanisms that affect the mixed-layer depth in the North Atlantic linked to the NAO. During positive NAO years, in the central North Atlantic the vertical mixing induced by strong westerly winds deepens the mixed layer. In the sub-Arctic and northern North Atlantic positive NAO years enhances the southerly transport of cold and fresh Arctic water which promotes strong stratification and the mixed layer shoals. This partially explains the decrease in average cumulative sums in the anomalies in NP in the EGC and CIC. These changes in response to NAO contrast with those in the Sargasso Sea, where negative NAO is associated

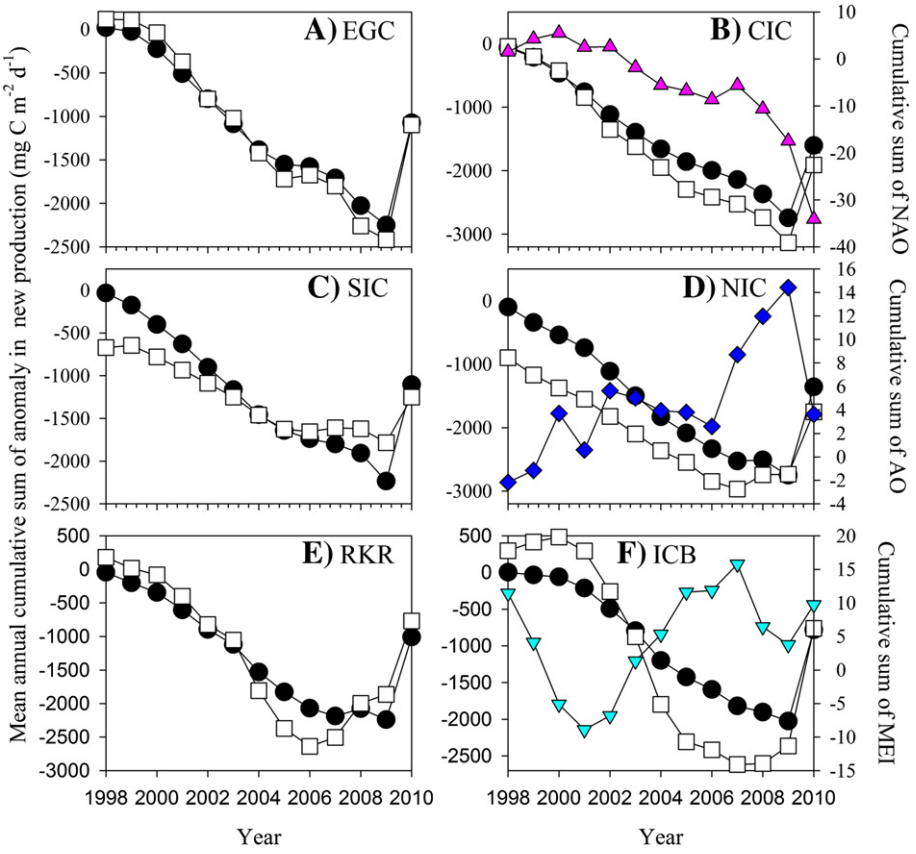

Fig. 8. Mean annual cumulative sums in the anomalies of new production for the WRM (filled circles) and VGPM (open squares) for (A.) East Greenland Current (EGC), (B.) Central Irminger Current (CIC), (C.) South Irminger Current (SIC), (D.) North Irminger Current (NIC), (E.) Reykjanes Ridge (RKR) and (F.) Iceland Basin (ICB). Climate indices are plotted in (B.), (D.) and (F.) for illustrative purposes. In (B.) pink triangles are mean annual cumulative sums in the anomalies of North Atlantic Oscillation Index (NAO). In (D.) blue diamonds are mean annual cumulative sums in the anomalies of Arctic Oscillation index (AO) and in (F.) cyanin inverted triangles are mean annual cumulative sums in the anomalies of Multivariate ENSO index (MEI).

Table 6
Pearson rank correlation between mean annual cumulative sums of the anomalies in NP from the WRM and VGPM, North Atlantic Oscillation (NAO), Arctic Oscillation (AO) and multiple ENSO index (MEI) for different hydrographic zones from 1998–2010. r is Correlation coefficient, P is level of significance. Significant correlations are given in bold; * indicates significant correlation at the 5% level; ** is 0.5% level and *** is 0.05% level.

Model	Bio-zone	NAO	AO	MEI
WRM	EGC	r = 0.569	−0.841	−0.390
		P = 0.042*	<0.0001***	0.188
WRM	CIC	r = 0.622	−0.841	−0.383
		P = 0.023*	<0.0001***	0.196
WRM	SIC	r = 0.545	−0.819	−0.387
		P = 0.054	0.001**	0.192
WRM	NIC	r = 0.516	−0.805	−0.440
		P = 0.071	0.001**	0.133
WRM	RKR	r = 0.481	−0.766	−0.463
		P = 0.096	0.002**	0.111
WRM	ICB	r = 0.522	−0.798	−0.513
		P = 0.067	0.001**	0.073
VGPM	EGC	r = 0.574	−0.831	−0.415
		P = 0.040*	<0.0001***	0.158
VGPM	CIC	r = 0.625	−0.815	−0.406
		P = 0.022*	0.001**	0.169
VGPM	SIC	r = 0.555	−0.745	−0.453
		P = 0.049*	0.003**	0.120
VGPM	NIC	r = 0.403	−0.735	−0.423
		P = 0.172	0.004**	0.150
VGPM	RKR	r = 0.379	−0.592	−0.531
		P = 0.202	0.033*	0.062
VGPM	ICB	r = 0.483	−0.692	−0.601
		P = 0.095	0.009**	0.030*

with a shift in storm tracks to the south, which causes a cooling of surface waters, a deepening of the winter mixed layer (Rodwell, Rowell, & Folland, 1999) and a paralleled increase in new production (Lipschultz, Bates, Carlson, & Hansell, 2002). Additionally, NP_{VGPM} also exhibited a significant correlation with NAO in the SIC. Since NAO is derived from differences in temperature in the NE Atlantic and $PP_{VGPM,}$ which was used to estimate $NP_{VGPM,}$ shows a greater sensitivity to changes in SST may explain why NP_{VGPM} exhibits higher correlation with climate indices.

Since 1998 the Arctic Oscillation has alternated between positive and negative, with a record negative phase in the winter of 2009–2010 (Foster, Cohen, Robinson, & Estilow, 2013). On an annual basis, the mean AO was negative in 1998, 2000–01, 2004–05 and 2009–10 and positive in 1999, 2002–03 and 2006–08. The positive phase of the AO brings ocean storms northwards, which makes the weather wetter in North Atlantic (Wang, Wang, Yang, & Lu, 2005). Pabi, van Dijken, and Arrigo (2008) showed that from 1998 to 2006 PP increased in open water areas of the Arctic and reached a maximum in 2006. They also showed that inter-annual variability in PP is tightly coupled to changes in sea ice and that variations in SST and incident irradiance contribute less to the variability in PP. When the springtime AO is strongly positive, snow melts earlier. When it is strongly negative, snow disappears later in the spring (Foster et al., 2013). Modelling studies have also suggested that during positive AO there will be an increase in PP and diatoms due the reduction in ice cover (Walsh, Dieterle, Maslowski, & Whitledge, 2004). By contrast, in the neighbouring Irminger Sea we observed a strong negative correlation between the average annual cumulative sum of the anomalies in AO and both NP_{VGPM}

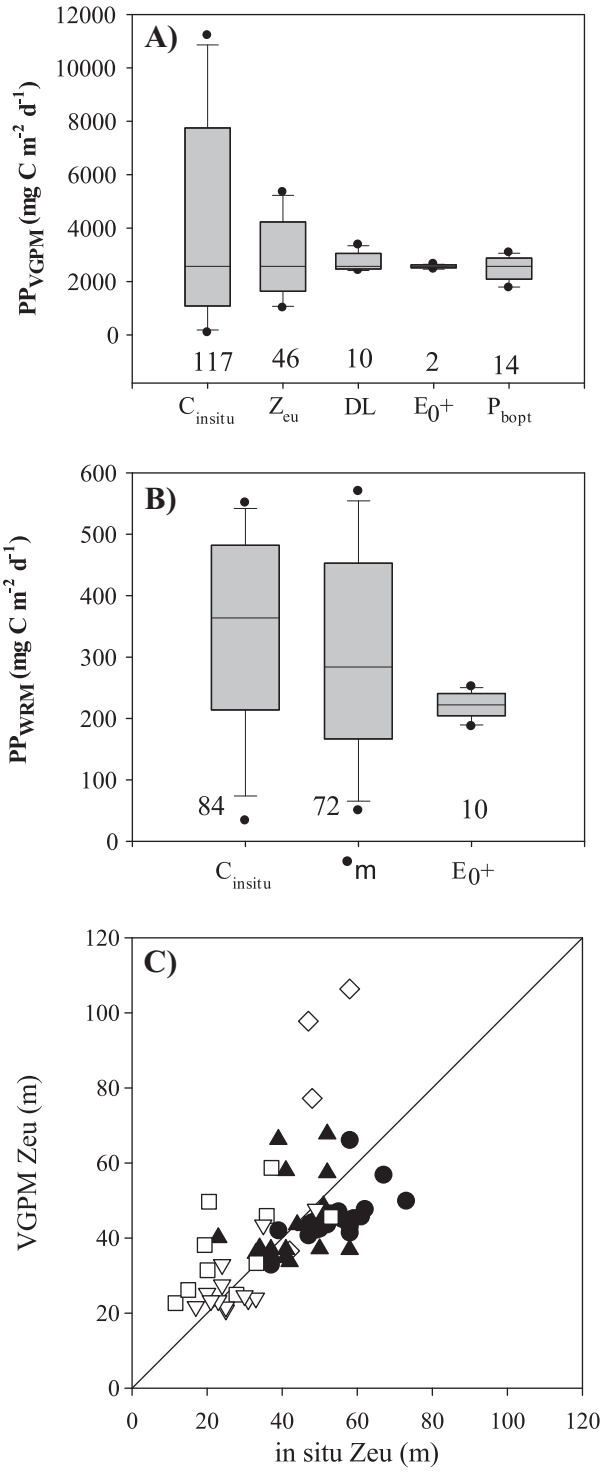

Fig. 9. Sensitivity analysis used to assess the degree to which algorithm variables affect the calculation of primary production (A.) PP_{VGPM} (B.) PP_{WRM} and (C.) euphotic depth (Z_{eu}) calculated from the VGPM algorithm against Z_{eu} calculated from in situ PAR profiles. In (A.) and (B.), the boundary of the box indicates the 25th and 75th percentile, the line within the box indicates the median, the whiskers above and below the box indicate the 90th and 10th percentiles and the dots outside the box are outlying points. The numbers given at the bottom of the plots are the mean errors incurred in calculating PP. In (C.), Filled circles are JC011 and JC037, open squares FISHES, filled triangles D264, open diamonds D267, inverted open triangles D261. In (A.) and (B.) C_{insitu} is in situ Chla, Z_{eu} is euphotic depth, DL is daylength, E_{0+} is irradiance just above the sea surface, P_b^{opt} is optimum photosynthetic rate, ϕ_m is maximum quantum yield of growth.

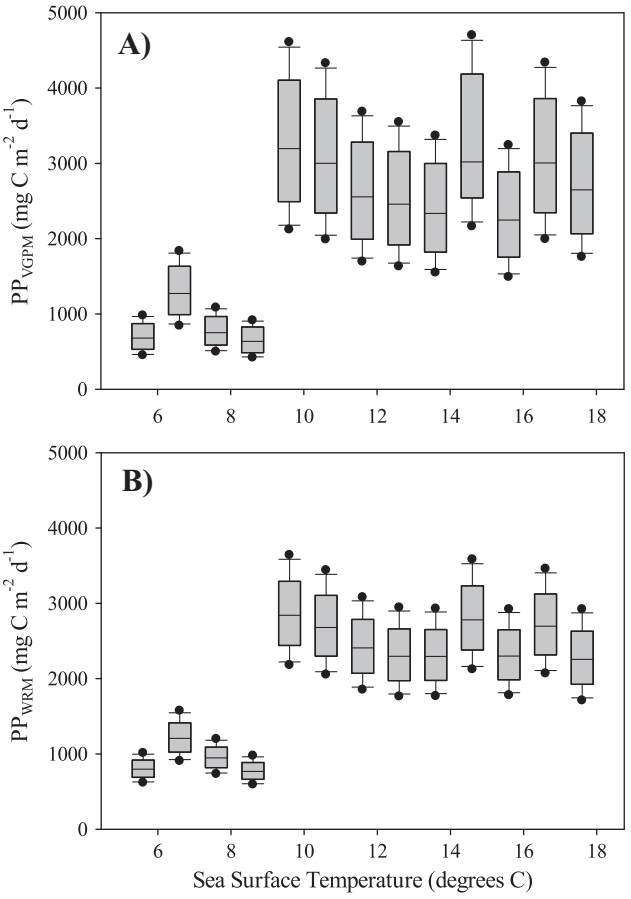

Fig. 10. Sensitivity analysis of the temperature dependency of (A.) P_b^{opt} on PP_{VGPM} and (B.) ϕ_m on PP_{WRM}.

and NP_{WRM} in all hydrographic zones, indicating that as AO becomes more positive, NP decreases (Fig. 8). This may be related to the fact that positive AO phase corresponds to the warm weather conditions further south (Wang et al., 2005), which would enhance stratification of the water column and thus reduce nutrient availability. This could also decrease NP (Fig. 8).

The effects of MEI on PP have been reported along the Californian Coast and as far North as British Columbia (Goes et al., 2004). More recently this has been extrapolated to the Global Ocean (Messie & Chavez, 2012). A decrease in global PP from 1998 to 2006 has been coupled to an increase in global SST as a result of the shift in MEI index (Behrenfeld et al., 2006). Goes et al. (1999, 2000) found that the primary driving force on NP in the sub-Arctic Pacific was the wintertime monsoon winds, which are stronger during *El Niño*. Based on remotely sensed estimates, they found that NP was highest in 1997 and 1998 corresponding with strong ENSO events and new production was lower when *La Niña* occurred. To further assess differences between NP models in relation to climate forcing, we compared the cumulative sums of the annual anomalies in MEI and NP_{VGPM} and NP_{WRM} in the six hydrographic zones (Fig. 8). The only significant correlation was between NP_{VGPM} and MEI in the ICB, which during *La Niña* (negative MEI) events from 1998–2003 caused a decrease in the average cumulative sum of the anomalies, whereas *El Niño* years (positive MEI) from 2004–2010, caused a reduction in the decrease followed by an increase in NP_{VGPM}. This correlation was not apparent for NP_{WRM}. Interestingly, in the ICB, NP_{VGPM} exhibited the greatest difference compared to NP_{WRM} and was 2.44 times higher (Fig. 6, Table 5). Since MEI and NAO are calculated from differences in SST and due to the sensitivity of the PP_{VGPM} to fluctuations in SST, NP_{VGPM} exhibited significant trends with NAO and MEI in more hydrographic zones than NP_{WRM}. It is therefore not surprising that

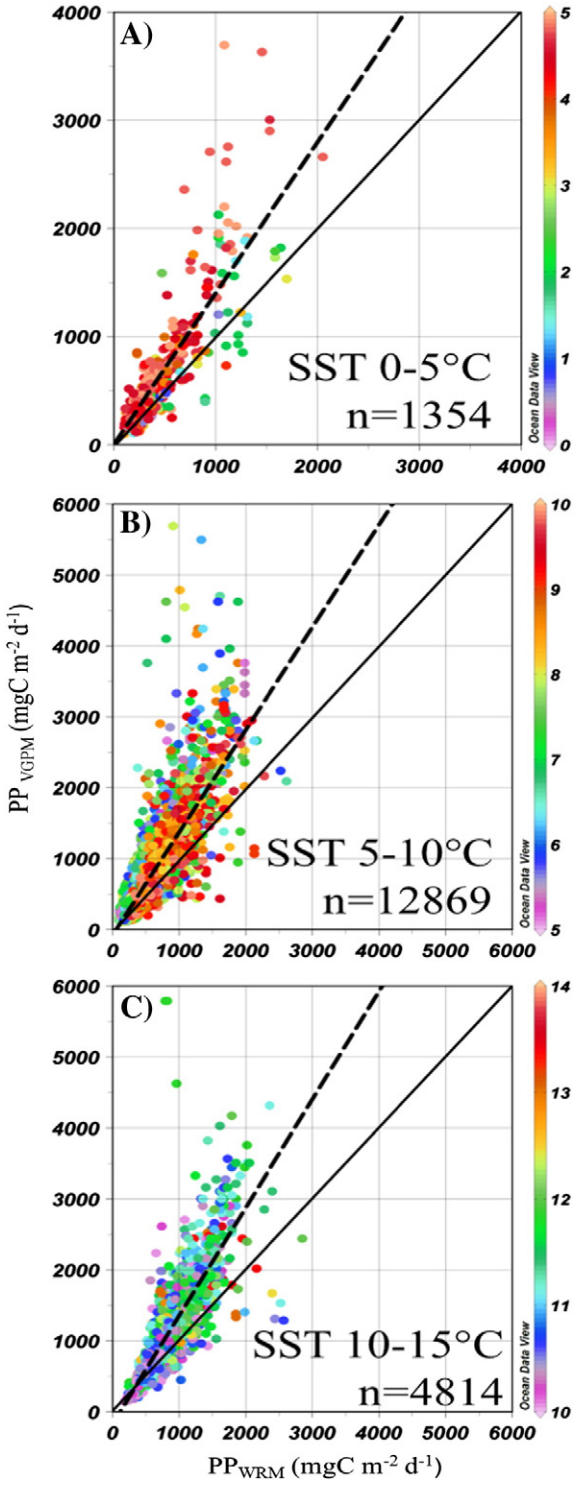

Fig. 11. Satellite estimates of primary production (mg C m^{-2} d^{-1}) for the VGPM and WRM extracted every 10 km from SW to NE transects through each hydrographic province (see Fig. 1 for location of transects) over the temperature range from (A.) 0–5°C, (B.) 5–10°C, (C.) 10–15°C. The colour bar is SST (°C). Dashed line is the regression line; solid line is 1:1 relationship.

Behrenfeld et al. (2006) reported a strong coupling between global PP_{VGPM} and MEI.

5. Conclusions

In situ ^{14}C and ^{15}N uptake measurements were used to assess the accuracy of the VGPM and WRM at estimating NP and PP in the northern North Atlantic. Both in situ and satellite estimates of Chla and SST were used as inputs to the models. Overall, the WRM was more accurate than VGPM at estimating both PP and NP which were within 30 and 10% of in situ data, respectively. The difference between models was greatest in the ICB where the temperature range was between 8 and 18 °C and lowest in the EGC where the temperature range was 5.5–15 °C. Both models however, had the highest annual PP in the ICB and the lowest annual PP in CIC.

The inter- and intra-variability in NP and PP calculated using SeaWiFS data from 1998 to 2010 in the northern North Atlantic with both models was also compared. PP and NP estimated using the VGPM was always higher than the WRM and the difference was greatest at low values. NP for the WRM was 20–70 gC m^{-2} yr^{-1}, whereas NP for the VGPM was 45–166 gC m^{-2} yr^{-1}. The effect of climate forcing on NP in contrasting hydrographic zones showed that the VGPM is more sensitive to variations in NAO and MEI compared to the WRM. Both models exhibited a significant negative correlation between the average annual cumulative sum in the anomalies of AO and NP.

The cause of differences in PP and NP using the WRM and VGPM were assessed. A sensitivity analysis on model input parameters illustrated that Chla has the greatest effect on both models, followed by Z_{eu} and P_b^{opt} in PP_{VGPM} and ϕ_m in PP_{WRM}. Since Chla was the same input for both models, errors in estimates of PP_{VGPM} were principally from Z_{eu} and the temperature dependency of P_b^{opt}, whereas for PP_{WRM} these were principally from ϕ_m. Over the temperature range found in the northern North Atlantic, the errors associated with estimating P_b^{opt}, resulted in PP_{VGPM} to be 15–40% higher than PP_{WRM} which propagated to a 50% difference between NP_{VGPM} and NP_{WRM} over 13 years of SeaWiFS data. The difference between the VGPM and WRM in each hydrographic zone was related to the temperature range encountered in each zone.

Based on these results, we recommend using the WRM of PP from Morel (1991) coupled with the NP model of Laws et al. (2000) to provide the most accurate satellite estimates of these parameters in the northern North Atlantic.

Acknowledgements

We thank the personnel aboard *RRS James Cook* and *RRS Discovery* during D261, D262, D264, D267, JC011 and JC037 field campaigns. We thank Claire Holeton, Denise Cummings, Victor Martinez-Vicente and Morvan Barnes for HPLC pigment data on Research cruises D264, D267, D261, JC011 and JC037. ECMWF data were provided by the British Atmospheric Data Centre (BADC). B.T., A.P.R., S.B.G. and G.H.T. were supported by the Natural Environment Research Council (NERC) UK Oceans 2025 research program. G.H.T. was also supported by the NERC-UK Marine Productivity thematic program Phase I (GST/02/2765) and NERC-UK consortium grant ECOMAR (NE/C513018/1). SeaWiFS and AVHRR data were processed by NERC Earth Observation Data Acquisition and Analysis Service (NEODAAS) Plymouth, UK. We are grateful to Reiner Schlitzer for use of Ocean Data View software version 4.0 to enable us to produce Fig. 11. We thank two anonymous referees for their comments that significantly improved this paper.

References

Abell, R.E., Brand, T., Dale, A.C., Tilstone, G.H., & Beveridge, C. (2013). Variability of particulate flux over the Mid-Atlantic Ridge. *Deep-Sea Research Part II-Topical Studies in Oceanography, 98*, 257–268.

Achterberg, E.P., Moore, C.M., Henson, S.A., Steigenberger, S., Stohl, A., Eckhardt, S., et al. (2013). Natural iron fertilization by the Eyjafjallajokull volcanic eruption. *Geophysical Research Letters, 40*, 921–926.

Allen, J.T., Brown, L., Sanders, R., Moore, C.M., Mustard, A., Fielding, S., et al. (2005). Diatom carbon export enhanced by silicate upwelling in the northeast Atlantic. *Nature, 437*, 728–732.

Alvarez-Salgado, X.A., Beloso, S., Joint, I., Nogueira, E., Chou, L., Perez, F.F., et al. (2002). New production of the NW Iberian shelf during the upwelling season over the period 1982–1999. *Deep-Sea Research Part I-Oceanographic Research Papers, 49*, 1725–1739.

Anderson, N.T. (2000). Diatoms, temperature and climatic change. *European Journal of Phycology*, *35*, 307–314.

Arbones, B., Figueiras, F.G., & Varela, R. (2000). Action spectrum and maximum quantum yield of carbon fixation in natural phytoplankton populations: Implications for primary production estimates in the ocean. *Journal of Marine Systems*, *26*, 97–114.

Azam, F. (1998). Microbial control of oceanic carbon flux: The plot thickens. *Science*, *280*, 694–696.

Babin, M., Therriault, J.C., & Legendre, L. (1991). Potential utilization of temperature in estimating primary production from remote-sensing data in coastal and estuarine waters. *Estuarine, Coastal and Shelf Science*, *33*, 559–579.

Bailey, S.W., & Werdell, P.J. (2006). A multi-sensor approach for the on-orbit validation of ocean color satellite data products. *Remote Sensing of Environment*, *102*, 12–23.

Barlow, R.G., Aiken, J., Moore, G.F., Holligan, P.M., & Lavender, S. (2004). Pigment adaptations in surface phytoplankton along the eastern boundary of the Atlantic Ocean. *Marine Ecology Progress Series*, *281*, 13–26.

Barlow, R.G., Cummings, D.G., & Gibb, S.W. (1997). Improved resolution of mono- and divinyl chlorophylls a and b and zeaxanthin and lutein in phytoplankton extracts using reverse phase C-8 HPLC. *Marine Ecology-Progress Series*, *161*, 303–307.

Barrie, A., & Lemley, M. (1989). Automated N-15/C-13 analysis of biological-materials. *American Laboratory*, *21*, 54–62.

Behrenfeld, M.J., Boss, E., Siegel, D.A., & Shea, D.M. (2005). Carbon-based ocean productivity and phytoplankton physiology from space. *Global Biogeochemical Cycles*, *19*.

Behrenfeld, M.J., & Falkowski, P.G. (1997). Photosynthetic rates derived from satellite-based chlorophyll concentration. *Limnology and Oceanography*, *42*, 1–20.

Behrenfeld, M.J., Maranon, E., Siegel, D.A., & Hooker, S.B. (2002). Photoacclimation and nutrient-based model of light-saturated photosynthesis for quantifying oceanic primary production. *Marine Ecology-Progress Series*, *228*, 103–117.

Behrenfeld, M.J., O'Malley, R.T., Siegel, D.A., McClain, C.R., Sarmiento, J.L., Feldman, G.C., et al. (2006). Climate-driven trends in contemporary ocean productivity. *Nature*, *444*, 752–755.

Bentsen, M., Drange, H., Furevik, T., & Zhou, T. (2004). Simulated variability of the Atlantic meridional overturning circulation. *Climate Dynamics*, *22*, 701–720.

Bouman, H.A., Platt, T., Sathyendranath, S., Li, W.K.W., Stuart, V., Fuentes-Yaco, C., et al. (2003). Temperature as indicator of optical properties and community structure of marine phytoplankton: implications for remote sensing. *Marine Ecology-Progress Series*, *258*, 19–30.

Campbell, J., Antoine, D., Armstrong, R., Arrigo, K., Balch, W., Barber, R., et al. (2002). Comparison of algorithms for estimating ocean primary production from surface chlorophyll, temperature, and irradiance. *Global Biogeochemical Cycles*, *16* (art. no.-1035).

Carr, M.E. (2002). Estimation of potential productivity in Eastern Boundary Currents using remote sensing. *Deep-Sea Research Part II-Topical Studies in Oceanography*, *49*, 59–80.

Carr, M.E., Friedrichs, M.A.M., Schmeltz, M., Aita, M.N., Antoine, D., Arrigo, K.R., et al. (2006). A comparison of global estimates of marine primary production from ocean color. *Deep-Sea Research Part II-Topical Studies in Oceanography*, *53*, 741–770.

Chavez, F.P., Service, S.K., & Buttrey, S. E. (1996). Temperature–nitrate relationships in the central and eastern tropical Pacific. *Journal of Geophysical Research-Oceans*, *101*, 20553–20563.

deYoung, B., Heath, M., Werner, F., Chai, F., Megrey, B., & Monfray, P. (2004). Challenges of modeling ocean basin ecosystems. *Science*, *304*, 1463–1466.

Dierssen, H. M. (2010). Perspectives on empirical approaches for ocean color remote sensing of chlorophyll in a changing climate. *Proceedings of the National Academy of Sciences of the United States of America*, *107*(40), 17073–17078, http://dx.doi.org/10.1073/pnas.0913800107.

Dierssen, H. M., & Smith, R. C. (2000). Bio-optical properties and remote sensing ocean color algorithms for Antarctic Peninsula waters. *Journal of Geophysical Research – Oceans*, *C11*, 26301–26312, http://dx.doi.org/10.1029/1999JC000296.

Dubinsky, Z. (1980). Light utilization efficiency in natural phytoplankton communities. In P. G. Falkowski (Ed.), *Primary productivity in the sea* (pp. 83–97). New York: Plenum Press.

Dugdale, R.C., Davis, C.O., & Wilkerson, F.P. (1997). Assessment of new production at the upwelling center at Point Conception, California, using nitrate estimated from remotely sensed sea surface temperature. *Journal of Geophysical Research-Oceans*, *102*, 8573–8585.

Dugdale, R.C., & Goering, J.J. (1967). Uptake of new and regenerated forms of nitrogen in primary productivity. *Limnology and Oceanography*, *12*, 196–206.

Dugdale, R.C., Morel, A., Bricaud, A., & Wilkerson, F.P. (1989). Modeling new production in upwelling centers—A case-study of modeling new production from remotely sensed temperature and color. *Journal of Geophysical Research-Oceans*, *94*, 18119–18132.

Eppley, R.W., & Peterson, B.J. (1979). Particulate organic-matter flux and planktonic new production in the deep ocean. *Nature*, *282*, 677–680.

Falkowski, P. (1988). Ocean productivity from space. *Nature*, *335*, 205.

Falkowski, P.G., Barber, R.T., & Smetacek, V. (1998). Biogeochemical controls and feedbacks on ocean primary production. *Science*, *281*, 200–206.

Figueiras, F.G., Arbones, B., & Estrada, M. (1999). Implications of bio-optical modeling of phytoplankton photosynthesis in Antarctic waters: Further evidence of no light limitation in the Bransfield Strait. *Limnology and Oceanography*, *44*, 1599–1608.

Foldvik, A., Aagaard, K., & Torresen, T. (1988). On the velocity-field of the East Greenland Current. *Deep-Sea Research Part A-Oceanographic Research Papers*, *35*, 1335–1354.

Foster, J.L., Cohen, J., Robinson, D.A., & Estilow, T.W. (2013). A look at the date of snowmelt and correlations with the Arctic Oscillation. *Annals of Glaciology*, *54*, 196–204.

Friedrichs, M.A.M., Carr, M. -E., Barber, R.T., Scardi, M., Antoine, D., Armstrong, R.A., et al. (2009). Assessing the uncertainties of model estimates of primary productivity in the tropical Pacific Ocean. *Journal of Marine Systems*, *76*, 113–133.

Frouin, R., & Pinker, R.T. (1995). Estimating Photosynthetically Active Radiation (Par) at the earths surface from satellite-observations. *Remote Sensing of Environment*, *51*, 98–107.

Goes, J.I., Gomes, H.D., Limsakul, A., Balch, W.M., & Saino, T. (2001). El Nino related interannual variations in biological production in the North Pacific as evidenced by satellite and ship data. *Progress in Oceanography*, *49*, 211–225.

Goes, J.I., Gomes, H.D., Limsakul, A., & Saino, T. (2004). The influence of large-scale environmental changes on carbon export in the North Pacific Ocean using satellite and shipboard data. *Deep-Sea Research Part II-Topical Studies in Oceanography*, *51*, 247–279.

Goes, J.I., Saino, T., Oaku, H., Ishizaka, J., Wong, C.S., & Nojiri, Y. (2000). Basin scale estimates of sea surface nitrate and new production from remotely sensed sea surface temperature and chlorophyll. *Geophysical Research Letters*, *27*, 1263–1266.

Goes, J.I., Saino, T., Oaku, H., & Jiang, D.L. (1999). A method for estimating sea surface nitrate concentrations from remotely sensed SST and chlorophyll a—A case study for the north Pacific Ocean using OCTS ADEOS data. *IEEE Transactions on Geoscience and Remote Sensing*, *37*, 1633–1644.

Gregg, W.W., & Carder, K.L. (1990). A simple spectral solar irradiance model for cloudless maritime atmospheres. *Limnology and Oceanography*, *35*, 1657–1675.

Hakkinen, S., & Rhines, P.B. (2004). Decline of subpolar North Atlantic circulation during the 1990s. *Science*, *304*, 555–559.

Hakkinen, S., & Rhines, P.B. (2009). Shifting surface currents in the northern North Atlantic Ocean. *Journal of Geophysical Research-Oceans*, *114*.

Heath, M.R., & Beare, D.J. (2008). New primary production in northwest European shelf seas, 1960–2003. *Marine Ecology Progress Series*, *363*, 183–203.

Henson, S.A., Dunne, J.P., & Sarmiento, J.L. (2009). Decadal variability in North Atlantic phytoplankton blooms. *Journal of Geophysical Research-Oceans*, *114*.

Henson, S.A., Sanders, R., Allen, J.T., Robinson, I.S., & Brown, L. (2003). Seasonal constraints on the estimation of new production from space using temperature–nitrate relationships. *Geophysical Research Letters*, *30*.

Henson, S.A., Sanders, R., Holeton, C., & Allen, J.T. (2006). Timing of nutrient depletion, diatom dominance and a lower-boundary estimate of export production for Irminger Basin, North Atlantic. *Marine Ecology-Progress Series*, *313*, 73–84.

Henson, S.A., Sanders, R., Madsen, E., Morris, P.J., Le Moigne, F., & Quartly, G.D. (2011). A reduced estimate of the strength of the ocean's biological carbon pump. *Geophysical Research Letters*, *38*.

Holliday, N.P., Waniek, J.J., Davidson, R., Wilson, D., Brown, L., Sanders, R., et al. (2006). Large-scale physical controls on phytoplankton growth in the Irminger Sea Part I: Hydrographic zones, mixing and stratification. *Journal of Marine Systems*, *59*, 201–218.

Hurrell, J.W., & Deser, C. (2009). North Atlantic climate variability: The role of the North Atlantic Oscillation. *Journal of Marine Systems*, *78*, 28–41.

IOC (1994). *Protocols for the Joint Global Ocean Flux Study (JGOFS) core measurements*. Paris, France: UNESCO.

Joint, I., Groom, S.B., Wollast, R., Chou, L., Tilstone, G.H., Figueiras, F.G., et al. (2002). The response of phytoplankton production to periodic upwelling and relaxation events at the Iberian shelf break: Estimates by the C-14 method and by satellite remote sensing. *Journal of Marine Systems*, *32*, 219–238.

Kamykowski, D., Reed, R.E., & Kirkpatrick, G.J. (1992). Comparison of sinking velocity, swimming velocity, rotation and path characteristics among 6 marine dinoflagellate species. *Marine Biology*, *113*, 319–328.

Laws, E.A. (2004). New production in the equatorial Pacific: A comparison of field data with estimates derived from empirical and theoretical models. *Deep-Sea Research Part I-Oceanographic Research Papers*, *51*, 205–211.

Laws, E.A., Falkowski, P.G., Smith, W.O., Ducklow, H., & McCarthy, J.J. (2000). Temperature effects on export production in the open ocean. *Global Biogeochemical Cycles*, *14*, 1231–1246.

Lipschultz, F., Bates, N.R., Carlson, C.A., & Hansell, D.A. (2002). New production in the Sargasso Sea: History and current status. *Global Biogeochemical Cycles*, *16*.

Maranon, E., Cermeno, P., Latasa, M., & Tadonleke, R.D. (2012). Temperature, resources, and phytoplankton size structure in the ocean. *Limnology and Oceanography*, *57*, 1266–1278.

Marra, J. (2009). Net and gross productivity: Weighing in with 14C. *Aquatic Microbial Ecology*, *56*, 123–131.

Marra, J., Trees, C.C., & O'Reilly, J.E. (2007). Phytoplankton pigment absorption: A strong predictor of primary productivity in the surface ocean. *Deep-Sea Research Part I-Oceanographic Research Papers*, *54*, 155–163.

McQuatters-Gollop, A., Mee, L. D., Raitsos, D. E., & Shapiro, G. I. (2008). Non-linearities, regime shifts and recovery: The recent influence of climate on Black Sea chlorophyll. *Journal of Marine Systems*, *74*, 649–658.

Messie, M., & Chavez, F.P. (2012). A global analysis of ENSO synchrony: The oceans' biological response to physical forcing. *Journal of Geophysical Research-Oceans*, *117*.

Milutinovic, S., & Bertino, L. (2011). Assessment and propagation of uncertainties in input terms through an ocean-color-based model of primary productivity. *Remote Sensing of Environment*, *115*, 1906–1917.

Moore, C.M., Lucas, M.I., Sanders, R., & Davidson, R. (2005). Basin-scale variability of phytoplankton bio-optical characteristics in relation to bloom state and community structure in the Northeast Atlantic. *Deep-Sea Research Part I-Oceanographic Research Papers*, *52*, 401–419.

Morel, A. (1988). Optical modelling of the upper ocean in relation to its biogenous matter content (Case I waters). *Journal of Geophysical Research-Oceans*, *93*, 10,749–710,768.

Morel, A. (1991). Light and marine photosynthesis—A spectral model with geochemical and climatological implications. *Progress in Oceanography*, *26*, 263–306.

Morel, A., Antoine, D., Babin, M., & Dandonneau, Y. (1996). Measured and modeled primary production in the northeast Atlantic (EUMELI JGOFS program): The impact of natural variations in photosynthetic parameters on model predictive skill. *Deep-Sea Research Part I-Oceanographic Research Papers*, *43*, 1273–1304.

Morel, A., & Berthon, J.F. (1989). Surface pigments, algal biomass profiles, and potential production of the euphotic layer—Relationships reinvestigated in view of remote-sensing applications. *Limnology and Oceanography*, *34*, 1545–1562.
Morin, P., Wafar, M.V.M., & Lecorre, P. (1993). Estimation of nitrate flux in a tidal front from satellite-derived temperature data. *Journal of Geophysical Research-Oceans*, *98*, 4689–4695.
Owens, N.J.P., & Rees, A.P. (1989). Determination of N-15 at submicrogram levels of nitrogen using automated continuous-flow isotope ratio mass-spectrometry. *Analyst*, *114*, 1655–1657.
Pabi, S., van Dijken, G.L., & Arrigo, K.R. (2008). Primary production in the Arctic Ocean, 1998–2006. *Journal of Geophysical Research-Oceans*, *113*.
Platt, T., Gallegos, C.L., & Harrison, W.G. (1980). Photoinhibition of photosynthesis in natural assemblage of marine phytoplankton. *Journal of Marine Research*, *38*, 687–701.
Porter, J., Kono, S., & Nielsen, T. (2005). Atmospheric correction errors under the Hawaii volcano: Possible solutions. In R.J.K.H.P.D. Frouin (Ed.), *Active and passive remote sensing of the oceans* (pp. 78–84).
Raven, J.A., & Geider, R.J. (1988). Temperature and algal growth. *New Phytologist*, *110*, 441–461.
Read, J.F., Pollard, R.T., Miller, P.I., & Dale, A.C. (2010). Circulation and variability of the North Atlantic Current in the vicinity of the Mid-Atlantic Ridge. *Deep-Sea Research Part I-Oceanographic Research Papers*, *57*, 307–318.
Reed, R. (1977). On estimating insolation over the ocean. *Journal of Physical Oceanography*, *7*, 482–485.
Rees, A.P., Joint, I., & Donald, K.M. (1999). Early spring bloom phytoplankton–nutrient dynamics at the Celtic Sea Shelf Edge. *Deep-Sea Research Part I-Oceanographic Research Papers*, *46*, 483–510.
Rees, A.P., Woodward, E.M.S., & Joint, I. (2006). Concentrations and uptake of nitrate and ammonium in the Atlantic Ocean between 60 degrees N and 50 degrees S. *Deep-Sea Research Part II-Topical Studies in Oceanography*, *53*, 1649–1665.
Robinson, C., Tilstone, G.H., Rees, A.P., Smyth, T.J., Fishwick, J.R., Tarran, G.A., et al. (2009). Comparison of in vitro and in situ plankton production determinations. *Aquatic Microbial Ecology*, *54*, 13–34.
Rodwell, M.J., Rowell, D.P., & Folland, C.K. (1999). Oceanic forcing of the wintertime North Atlantic Oscillation and European climate. *Nature*, *398*, 320–323.
Saba, V.S., Friedrichs, M.A.M., Antoine, D., Armstrong, R.A., Asanuma, I., Behrenfeld, M.J., et al. (2011). An evaluation of ocean color model estimates of marine primary productivity in coastal and pelagic regions across the globe. *Biogeosciences*, *8*, 489–503.
Saba, V.S., Friedrichs, M.A.M., Carr, M. -E., Antoine, D., Armstrong, R.A., Asanuma, I., et al. (2010). Challenges of modeling depth-integrated marine primary productivity over multiple decades: A case study at BATS and HOT. *Global Biogeochemical Cycles*, *24*.
Sanders, R., Brown, L., Henson, S., & Lucas, M. (2005). New production in the Irminger Basin during 2002. *Journal of Marine Systems*, *55*, 291–310.
Sarmiento, J.L., Hughes, T.M.C., Stouffer, R.J., & Manabe, S. (1998). Simulated response of the ocean carbon cycle to anthropogenic climate warming. *Nature*, *393*, 245–249.
Sathyendranath, S. (2000). Remote sensing of ocean colour in coastal and other optically-complex waters. In V. Stuart (Ed.), *IOCCG report* (pp. 1–137). Canada: Bedford Institute of Oceanography.
Sathyendranath, S., Gouveia, A.D., Shetye, S.R., Ravindran, P., & Platt, T. (1991). Biological-control of surface-temperature in the Arabian Sea. *Nature*, *349*, 54–56.
Saux-Picart, S., Sathyendranath, S., Dowell, M., Moore, T., & Platt, T. (2014). Remote sensing of assimilation number for marine phytoplankton. *Remote Sensing of Environment*, *146*, 87–96.
Siegel, D.A., Westberry, T.K., O'Brien, M.C., Nelson, N.B., Michaels, A.F., Morrison, J.R., et al. (2001). Bio-optical modeling of primary production on regional scales: the Bermuda BioOptics project. *Deep-Sea Research Part II-Topical Studies in Oceanography*, *48*, 1865–1896.
Silio-Calzada, A., Bricaud, A., Uitz, J., & Gentili, B. (2008). Estimation of new primary production in the Benguela upwelling area, using ENVISAT satellite data and a model dependent on the phytoplankton community size structure. *Journal of Geophysical Research-Oceans*, *113*.
Smith, W.O., Codispoti, L.A., Nelson, D.M., Manley, T., Buskey, E.J., Niebauer, H.J., et al. (1991). Importance of phaeocystis blooms in the high-latitude ocean carbon-cycle. *Nature*, *352*, 514–516.
Smyth, T.J., Tilstone, G.H., & Groom, S.B. (2005). Integration of radiative transfer into satellite models of ocean primary production. *Journal of Geophysical Research-Oceans*, *110*.
Sokal, R.R., & Rolf, F.J. (1997). *Biometry*. New York: W.H. Freeman and Company.
Tilstone, G.H., Figueiras, F.G., Lorenzo, L.M., & Arbones, B. (2003). Phytoplankton composition, photosynthesis and primary production during different hydrographic conditions at the Northwest Iberian upwelling system. *Marine Ecology-Progress Series*, *252*, 89–104.
Tilstone, G.H., Smyth, T.J., Gowen, R.J., Martinez-Vicente, V., & Groom, S.B. (2005). Inherent optical properties of the Irish Sea and their effect on satellite primary production algorithms. *Journal of Plankton Research*, *27*, 1127–1148.
Tilstone, G., Smyth, T., Poulton, A., & Hutson, R. (2009). Measured and remotely sensed estimates of primary production in the Atlantic Ocean from 1998 to 2005. *Deep-Sea Research Part II-Topical Studies in Oceanography*, *56*, 918–930.
Traganza, E.D., Nestor, D.A., & McDonald, A.K. (1980). Satellite-observations of a nutrient upwelling off the coast of California. *Journal of Geophysical Research-Oceans and Atmospheres*, *85*, 4101–4106.
Volpe, G., Santoleri, R., Vellucci, V., Ribera d'Alcala, M., Marullo, S., & D'Ortenzio, F. (2007). The colour of the Mediterranean Sea: Global versus regional bio-optical algorithms evaluation and implication for satellite chlorophyll estimates. *Remote Sensing of Environment*, *107*(4), 625–638, http://dx.doi.org/10.1016/j.rse.2006.10.017.
Waldron, H.N., & Probyn, T.A. (1992). Nitrate supply and potential new production in the Benguela upwelling system. *South African Journal of Marine Science-Suid-Afrikaanse Tydskrif Vir Seewetenskap*, *12*, 29–39.
Walsh, J.J., Dieterle, D.A., Maslowski, W., & Whitledge, T.E. (2004). Decadal shifts in biophysical forcing of Arctic marine food webs: numerical consequences. *Journal of Geophysical Research-Oceans*, *109*.
Wang, D.X., Wang, C.Z., Yang, X.Y., & Lu, J. (2005). Winter Northern Hemisphere surface air temperature variability associated with the Arctic Oscillation and North Atlantic Oscillation. *Geophysical Research Letters*, *32*.
Waniek, J.J., & Holliday, N.P. (2006). Large-scale physical controls on phytoplankton growth in the Irminger Sea, Part II: Model study of the physical and meteorological preconditioning. *Journal of Marine Systems*, *59*, 219–237.
Yentsch, C.S., Yentsch, C.M., Phinney, D.A., Lapointe, B.E., & Yentsch, S.F.W. (2004). The odyssey of new production. *Journal of Experimental Marine Biology and Ecology*, *300*, 15–30.
Yool, A., Martin, A.P., Fernandez, C., & Clark, D.R. (2007). The significance of nitrification for oceanic new production. *Nature*, *447*, 999–1002.
Zhai, L., Platt, T., Tang, C., Sathyendranath, S., & Walne, A. (2013). The response of phytoplankton to climate variability associated with the North Atlantic Oscillation. *Deep-Sea Research Part II-Topical Studies in Oceanography*, *93*, 159–168.